

# Upgrades to the Fluorescence Detectors of the Pierre Auger Observatory



THE UNIVERSITY  
*of*ADELAIDE

**Tristan William Sudholz**

School of Physical Sciences  
University of Adelaide

This dissertation is submitted for the degree of  
*Doctor of Philosophy*

February, 2020



# Declaration

I, Tristan William Sudholz, certify that this work contains no material which has been accepted for the award of any other degree or diploma in any university or other tertiary institution and, to the best of my knowledge and belief, contains no material previously published or written by another person, except where due reference has been made in the text. In addition, I certify that no part of this work will, in the future, be used in a submission for any other degree or diploma in any university or other tertiary institution without the prior approval of the University of Adelaide and where applicable, any partner institution responsible for the joint-award of this degree.

I give consent to this copy of my thesis, when deposited in the University Library, being made available for loan and photocopying, subject to the provisions of the Copyright Act 1968.

I also give permission for the digital version of my thesis to be made available on the web, via the University's digital research repository, the Library catalogue and also through web search engines, unless permission has been granted by the University to restrict access for a period of time.

---

Tristan William Sudholz



# **Abstract**



# Acknowledgements



# Contents

<b>Nomenclature</b>	<b>xi</b>
<b>Introduction</b>	<b>1</b>
<b>1 Cosmic-Rays</b>	<b>3</b>
1.1 History of Cosmic-Rays . . . . .	3
1.2 Energy Spectrum and Mass composition . . . . .	3
1.3 Production Method and Sources . . . . .	3
<b>2 Detection of Cosmic-rays</b>	<b>7</b>
2.1 Extensive Air Showers . . . . .	7
2.2 Fluorescence Production . . . . .	7
2.3 Atmospheric Effects . . . . .	7
2.4 Detectors and History . . . . .	7
<b>3 Pierre Auger Observatory</b>	<b>9</b>
3.1 Surface Detector . . . . .	9
3.1.1 AugerPrime . . . . .	9
3.2 Fluorescence Detector . . . . .	9
3.2.1 Photomultiplier Tubes . . . . .	12
3.3 Communication System and CDAS . . . . .	12
3.4 Event Reconstruction . . . . .	12
3.4.1 Surface Detector . . . . .	12
3.4.2 Fluorescence Detector . . . . .	12
3.5 Enhancements and future upgrades . . . . .	12
<b>4 EAS Selection Efficiency with Increased NSB</b>	<b>13</b>
4.1 Motivation . . . . .	13
4.2 Selection Efficiency . . . . .	15
4.3 Resolution and Bias . . . . .	15
4.3.1 Comparing Simulated Data to Real Data . . . . .	17
4.4 EAS Track Length in the FD's . . . . .	17
<b>5 Quantifying Characteristics of the FD PMT</b>	<b>25</b>
5.1 PMT Linearity . . . . .	25
5.1.1 Neutral Density Filters . . . . .	25
5.1.2 Two LED Method . . . . .	28
5.2 Effects of Temperature on PMT Gain . . . . .	28

<b>6 Computer Simulation of FD PMT</b>	<b>33</b>
6.1 Method and Theory . . . . .	33
6.1.1 Theoretical value of Gain Variance? . . . . .	33
6.2 Results of PMT Gain Variance Simulation . . . . .	34
6.3 Simulation of Gain Variance Method . . . . .	34
6.4 FD FLT under different NSB levels . . . . .	34
<b>7 Measuring FD PMT Gain Variance with CalA Data</b>	<b>41</b>
7.1 Using CalA to measure relative changes in Gain Variance . . . . .	41
7.2 Electronic Noise . . . . .	42
7.3 Pairs Method . . . . .	42
7.3.1 Results . . . . .	46
7.4 Averaging Sets of Traces Method . . . . .	46
7.4.1 Results . . . . .	46
7.5 Result of Averaging Sets of Traces Method with Least Trimmed Squares	46
7.6 Result of Averaging Sets of Traces Method using Noise Distribution .	54
7.7 Attempts to measure Gain Variance directly in the Lab . . . . .	54
<b>8 Laboratory Simulation of FD shift</b>	<b>57</b>
<b>9 Evaluation of Cloud Camera Cuts</b>	<b>59</b>
<b>10 Conclusion</b>	<b>61</b>
10.1 Future Work . . . . .	61

# Nomenclature

PAO	Pierre Auger Observatory
EAS	Extensive Air Shower
NSB	Night Sky Background
PE	Photo-electron
FD	Fluorescence Detector
SD	Surface Detector
PMT	Photomultiplier Tube
FLT	First Level Trigger



# Introduction

- Define Cosmics Rays.
- The origins of the highest energy cosmic-rays still unknown.
- First detection by Pierre Auger in 1937 and the current detector looking at these energies is the Pierre Auger Observatory.
- Hybrid experiment containing both surface detectors and fluorescence detectors
- Surface detector has nearly 100% up-time while the fluorescence detectors only have 15% up-time.
- \*\*\*\* Proposal to extend the fluorescence detector up-time. To achieve this will have to operate while the moon is above the horizon. This will increase the level NSB and will have the PMTs run under a reduced gain to compensate. \*\*\*\*
- Photomultiplier Tubes are used as pixels within the camera of the fluorescence detectors and the aim of these thesis is to quantify the characteristics of the PMT under the reduced gain and increased.
- Outline a Summary of each chapter.

Cosmic-rays are particles that originate outside of the Earth atmosphere. These particles can be photons, hadronic or leptonic in nature [ref?]. In this thesis, when mentioning cosmic-rays I will mean the hadronic component unless specified otherwise. Cosmic-rays have been measured over a large range of energies (over 6 decades in energy) and it has many interesting features have been observed in this energy spectrum. One of the longest running mysteries is what happens at the highest energy. Since the first detection of extensive air showers by Pierre Auger in 1937 [ref], many different experiments have endeavoured to solve this mystery. The Pierre Auger Observatory [ref] is currently in operation to observe cosmic-rays at the highest energies.

The Pierre Auger Observatory is a hybrid experiment consisting of both surface detectors and fluorescence detectors. (Outline location) The surface detector has a nearly 100% operation up-time ref while the fluorescence detectors only 15% operation up-time [ref]. (Outline how PAO detects cosmic-rays, just need a brief summary).

A current proposal to extend the fluorescence detector operation up-time. Extended up-time would be beneficial as the fluorescence detectors image the entire extensive air shower and would increase the number of showers observed through out yearly observation. To achieve the extended operation the fluorescence detectors would have to be operated while the moon is above the horizon. While the moon is up, this would increase the Night Sky Background level and to compensate the Photomultiplier Tubes acting as the camera pixels would have to be run under reduced gain.

The aim of this thesis is to quantify the characteristics of the Photomultiplier Tubes operating under this reduced gain and outline any operation strategies. Outline of each chapter is as follows:

- Chapter 1: Cosmic-rays  
Does this work as a new line
- Chapter 2: Detection of Cosmic-Rays  
Add text here
- Chapter 3: The Pierre Auger Observatory  
Add text here
- Chapter 4 : EAS Selection Efficiency with Increased NSB  
Add text here
- Chapter 5 : Quantifying Characteristics of the FD PMT  
Add text here
- Chapter 6 : Computer Simulation of the FD PMT  
Add text here
- Chapter 7 : Measuring Gain Variance of the FD PMT with CalA data  
Add text here
- Chapter 8 : Laboratory Simulation of FD Shifts  
Add text here
- Chapter 9 : Effectiveness of Cloud Camera Cuts  
Add text here
- Chapter 10: Conclusion  
Future Work

# Chapter 1

## Cosmic-Rays

### 1.1 History of Cosmic-Rays

First detection of ionizing radiation.

1785: Coulomb found that electroscopes can spontaneously discharge by the action of the air and not by defective insulation

1835: Faraday confirms the observation by Coulomb, with better insulation technology

1879: Crookes measures that the speed of discharge of an electroscope decreased when pressure was reduced

### 1.2 Energy Spectrum and Mass composition

Cosmic-rays have been detected over a large range of energies from GeV ( $10^9$  eV) to above EeV ( $10^{18}$  eV). Spectrum in Figure 1.1 shows the break at the knee and ankle and which type of experiments are most suited to measurement each part. Cosmic-ray spectrum starts out at  $E^{-2}$  and can be as steep as  $E^{-2.7}$  at the highest energies.

Cosmic-rays can consist of protons to iron.

CR spectrum has many features. Main features are the knee, second knee and ankle. The knee is around  $3 \times 10^{15}$ .

Pierre Auger Observatory measurement of isotropy that shows that the cosmic-ray spectrum changes from predominately galactic to extra-galactic at the ankle.

Predicted Greisen-Zatsepin-Kuzmin (GZK) cut-off about  $6 \times 10^{19}$ . Cosmic-rays above this energy are theorised to interact with the cosmic microwave background radiation. Greisen independently of Kuz'man and Zatsepin all predicted this energy loss.

Pierre Auger Observatory measurement of  $X_{\text{max}}$  and the second moment  $\sigma(X_{\text{max}})$  has mass composition information as well how this changes as a function of energy.

### 1.3 Production Method and Sources

- Bottom-Up Acceleration
  - Supernova explosions
  - AGN jets
  - other energetic processes

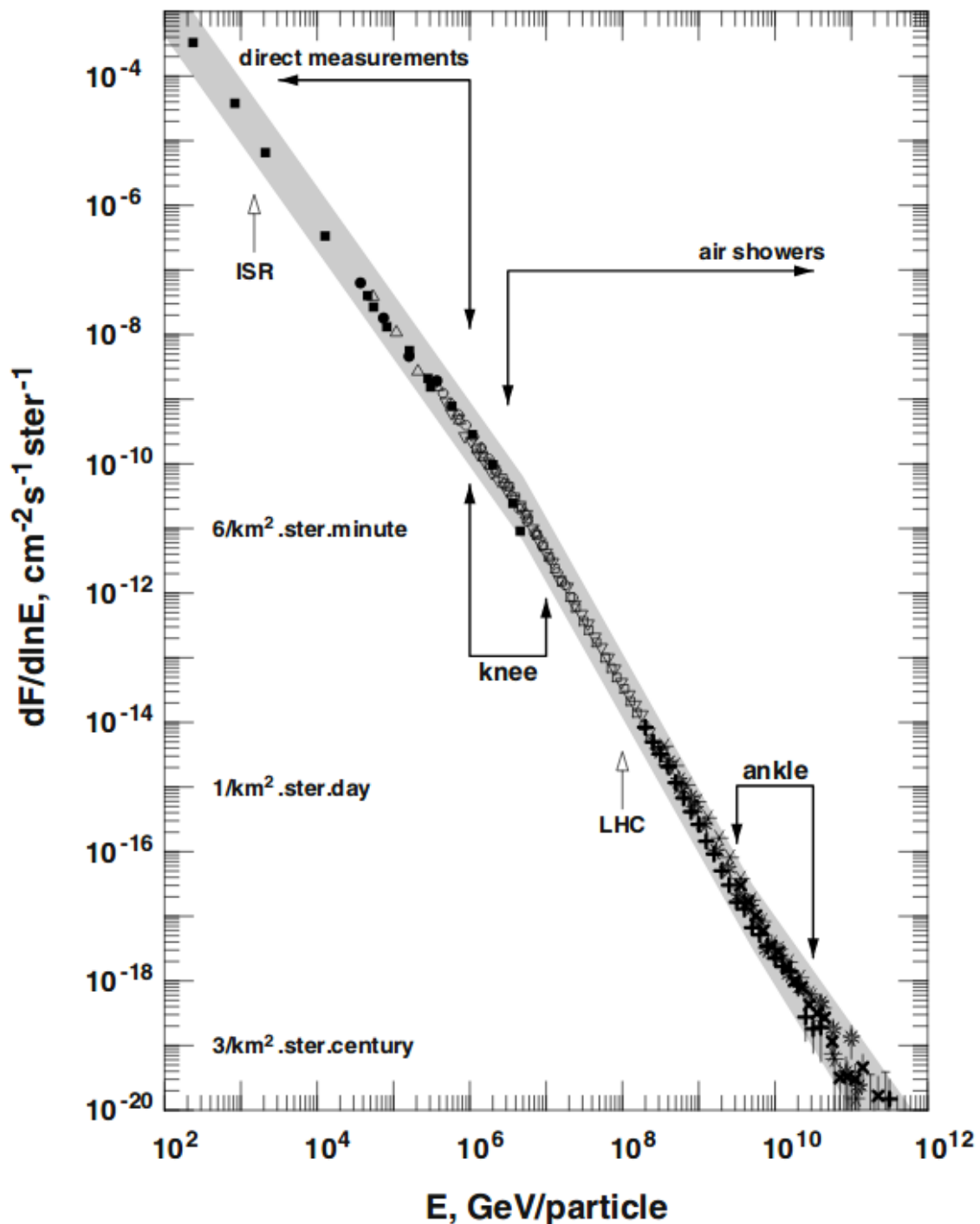


**Figure 1.1:** Measured energy spectrum of cosmic-rays from 100 GeV up to the highest detected energy.

dark matter annihilations.

- Top-Down Acceleration

Decay of massive relic particles

Typically associated with new physics beyond the standard model



# Chapter 2

## Detections of Cosmic-Rays

### 2.1 Extensive Air Showers

Use Earth's atmosphere as an interaction medium. Primary particle interacts with the molecules in the atmosphere to produce a cascade of secondary particles. This cascade of particles is referred to as an Extensive Air Shower (EAS). Hadronic primaries can produce pions, muons and other stuff. Mixture of a hadronic core with an electromagnetic component from the decay of  $\pi^0$ .

Shower profile has particles produced until energy of individual secondary particles drop below the ionization threshold. Therefore the shower will reach a point of maximum particle number then will drop off.

### 2.2 Fluorescence Production

The charge particles of EAS interact with the nitrogen molecules in the atmosphere. This interaction turns the nitrogen molecule dipole like and when the nitrogen returns to a ground state, a photon is emitted. This emitted photon is termed fluorescence light. Fluorescence light is emitted isotropically and typically in the UV band (between 300 and 400 nm). \*\*\* Show wavelength profile \*\*\*

### 2.3 Atmospheric Effects

### 2.4 Detectors and History

Early Experiments:

Volcano Ranch

Haverah Park

SUGAR

Yakutsk array is located in Russia and has been operating in different forms since 1967. The array reached a maximum collecting area of  $17 \text{ km}^2$  around 1990. Recently it has been reconfigured to have a collection area of  $8 \text{ km}^2$  to study lower energy cosmic-rays.

Akeno Gaint Air Shower Array (AGASA) is located in Tokyo, Japan. Operating at an average altitude of 667 m above sea level from 1990 to 2004. The array consist of



**Figure 2.1:** Diagram of Cosmic-ray Extensive Air Showers.

over one hundred scintillator detectors covering  $100 \text{ km}^2$  \*\*\*check this\*\*\*. The timing measurements and data collection is achieved via interconnected optical fibers.

The Fly's Eye was the first successful air fluorescence detector operating from 1981 to 1993 at the Dugway Proving Grounds in Utah, USA. Fly's Eye achieved a time averaged aperture of about  $100 \text{ km}^2 \text{sr}$  at the highest energies, considering it only operated on clear moonless nights.

HiRes improved on the Fly's Eye design by advancing resolution and sensitivity, This was achieved by increasing the telescope effective mirror area to  $3.8 \text{ m}^2$  and reducing the camera pixel angular diameter to  $1^\circ$ .

# **Chapter 3**

## **Pierre Auger Observatory**

Science Goals of the Pierre Auger Observatory is to probe the origins and characteristics of cosmic rays above  $10^{17}$  eV and to study the interactions of the most energetic particles observed in nature.

The Pierre Auger Observatory (PAO) is an hybrid detector that is located near Malargüe in the Mendoza Province, Argentina. PAO consists of 1660 Cherenkov water detector spread over 3000 km<sup>2</sup> by 24 fluorescence telescopes.

### **3.1 Surface Detector**

The surface array consists of 1660 water Cherenkov tanks. The majority of tanks are configured with a spacing of 1500 metres while there is a small subset of tanks in front of the fluorescence telescopes at the Coihueco site with spacing of 750 metres.

The surface array has a duty cycle of nearly 100% and the maintenance cycle is so that no more then 20 tanks are down at any one time.

#### **3.1.1 AugerPrime**

### **3.2 Fluorescence Detector**

There are four fluorescence detector site surrounding the surface array. At each fluorescence detector site there are six telescopes covering 180° in azimuth and 30° in elevation. At one site there are three extra telescopes with slightly greater then 90° in azimuth and cover 30° to 60° in elevation.

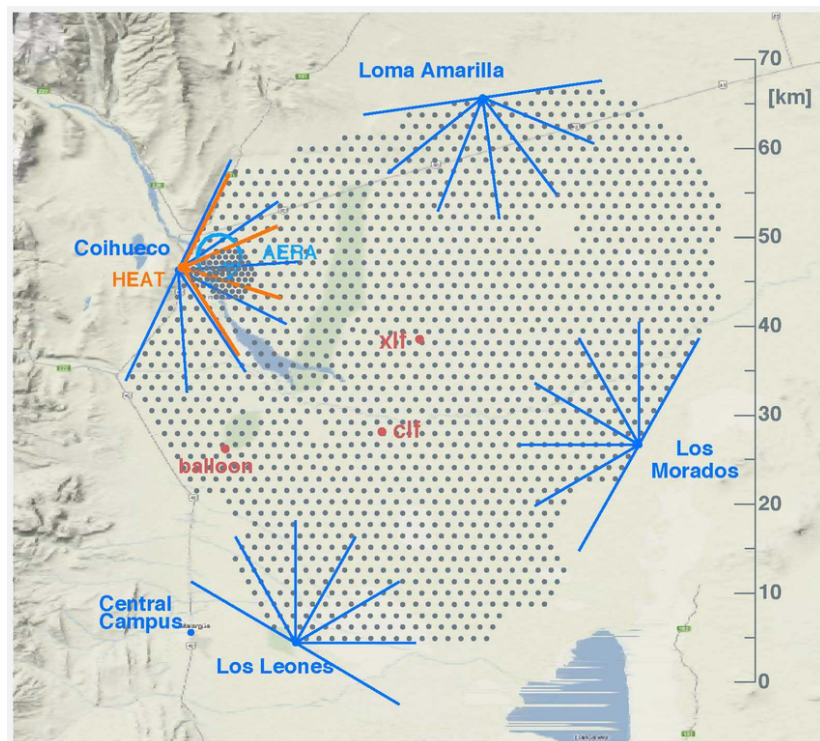


**Figure 3.1:** Image of layout of Pierre Auger Observatory located near Malargüe, Argentina.



**Figure 3.2:** Image of one of the fluorescence detector site (background) and one of the surface detectors (foreground).



Figure 3.3: Basic schematic of a surface detector.



Figure 3.4: Basic schematic of a fluorescence telescope.

### **3.2.1 Photomultiplier Tubes**

## **3.3 Communication System and CDAS**

## **3.4 Event Reconstruction**

### **3.4.1 Surface Detector**

### **3.4.2 Fluorescence Detector**

## **3.5 Enhancements and future upgrades**

# Chapter 4

## EAS Selection Efficiency with Increased NSB

### 4.1 Motivation

The FD shifts are typically organised for night with the illuminated fraction of the moon less than 70% and can be operated longer than 3 hours of moon below the horizon. The Fd telescope shutters are then opened when the sun is below -18° of the horizon (astronomical twilight), the average variance of the camera PMTs less than 100 ADC<sup>2</sup> and individual PMTs less than 2000 ADC<sup>2</sup>. Two calculations where done by the collaboration to estimate the theoretical up time of the FD's. Before 2012 the theoretical calculations looked like:

Theoretical up time	22%
Loss due to short nights (< 3 hrs)	-2%
Loss due to bad weather or fails	-5%
Total measurement time	15%

For context the measured ADC<sup>2</sup> for typically observed Night Sky Background (NSB) with no moon, quarter moon and full moon/twilight is:

Condition	$\sigma^2$ [ADC <sup>2</sup> ]	I <sub>a</sub> [ $\mu$ A]
no moon	25	0.5
quarter moon	250	5
full moon/twilight	2500	50

These values are measured under the standard operation of the FD's. Further within this thesis I will investigate lower the gain on the PMTs to reduce the variance and current that their under. A lower current when observing under moonlight would help make sure that the PMT lifespans are not changed by the increased in NSB.

The signal that the FD's observe is AC coupled, which means the mean signal of the NSB is zero. Instead the variance around zero is calculated and is directly proportional to the fluctuations in the NSB. The average value of the NSB measured by POA at Malargue is:

$$\sigma^2 \sim 25 \text{ ADC}^2 \quad (4.1)$$

The variance in  $\text{ADC}^2$  can be converted into photons seen at the aperture by using:

$$\sigma_{pe}^2 = [\sigma_{\text{ADC}}^2]^{\text{sky}} / A_G^2 \quad (4.2)$$

$$n_{\text{ph}} = \frac{\sigma_{pe}^2}{(1 + V_G)} \quad (4.3)$$

where  $\sigma_{pe}$  is the standard deviation of the photo-electron count,  $n_{\text{ph}}$  is the photon count and  $A_G$  is equal to:

$$A_G = \frac{1}{C_{\text{FD}} \cdot f \cdot Q} \quad (4.4)$$

where

$A_G$  is the absolute gain (ADC/photo-electron)

$C_{\text{FD}}$  is the FD pixel calibration constant.

$Q$  is the Quantum efficiency of the PMT.

$f$  is the efficiency if the telescope optics.

/\*— Find reference to number below —\*/

Assuming typical measured values for  $C_{\text{FD}}$ ,  $Q$  and  $f$  shown in:

$C_{\text{FD}}$	4.5 photons/ADC
$Q$	0.29
$f$	0.465

**Table 4.1**

Therefore  $A_G$  can be calculated from Eq. 4.4 and using the values from Table 4.1. If  $\sigma_{\text{ADC}}^2 = 25 \text{ ADC}^2$ , through the calculations  $n_{\text{ph}} = 23 \text{ photons / 100 ns}$ . The calculations to work out the  $\text{RMS}_{\text{ph}}$  from the measured variance in  $\text{ADC}^2$  is as follows:

$$\text{RMS}_{\text{ph}} = C_{\text{FD}} \times \sqrt{\text{ADC}^2} \quad (4.5)$$

From all of the equations stated above I have outlined a table showing the expected photon count at the aperture per 100 ns from the measured variance ( $\text{ADC}^2 / 100 \text{ ns}$ ).

Variance ( $\text{ADC}^2 / 100 \text{ ns}$ )	$\log_{10}(V/\text{ADC}^2)$	Photons/100 ns	RMS (Photons/100 ns)
25	1.40	22.7	22.5
178	2.25	161.4	60
259	2.40	226.7	71.2
1000	3.00	907.0	142.3

- Need graph of expected variance in  $\text{ADC}^2$  for the moon above the horizon for different phases.

- Want to increase the duty cycle of FD by measuring EAS under moonlight. Most likely observe under quarter to half moon. This will increased the NSB upto a factor of 10.

- The aim of increasing the duty cycle of FD is too measure more EAS at the highest energy band ( $> 10^{19.5} \text{ eV}$ ).

- Need more statistics at highest energy band to complement SD measurements.

## 4.2 Selection Efficiency

I investigated evaluating increasing the NSB by different factors on event reconstruction seen the FD's through a couple of different methods. The main increase of NSB will from observing while the moon is above the horizon. The two methods involved simulating increased NSB on measured data and with simulating. The measured data had increased noise introduced across the entire signal trace and I have labelled as the smearing method.

Selection Efficiency for the two methods are calculated via:

$$\text{Efficiency} = N_{\text{Selected}} / N_{\text{total}} \quad (4.6)$$

where for the Smearing method  $N_{\text{total}}$  is the total number of measured EAS events at standard NSB levels and  $N_{\text{Selected}}$  is the number of events after being reconstructed and passing the quality cuts with the increased NSB. For the simulations,  $N_{\text{total}}$  is the total number of simulated events before **need to check whether its the number of simulations before triggering or number of triggered events at standard NSB. Pretty sure the comparison is done with no. of simulated event at standard NSB.**

Smearing method involves taking the raw fluorescence telescope EAS shower events that would pass reconstruction and quality cuts and adding addition variance in ADC<sup>2</sup> equivalent to an increased NSB from moonlight to the FD pixel signal traces. The shower events are then reconstructed and passed through the same quality cuts. This a repartition of a similar method that M. Unger had preformed in **2012**. Also **need to refer to the study done by Brue and Andrew Smith around 1999**. This was done so a deeper analysis could be preformed to understand the underlying mechanics.

The simulations were done using the simulation modules for the FD's within the OffLine analysis programs. The EAS profiles were generated within CONEX and the original showers were generated through CORSIKA. The NSB was added to the EAS profiles before the FD are triggered. A hybrid trigger is used to involve the SD but the SD is simulated in a simple way just to get a simulated core position.

The smearing method was originally used as a proof of concept to show that EAS showers could still be reconstructed with the increased NSB. The limitation was that EAS were used that already triggered the FD's normally. The full simulation using CONEX showers was used to full test trigger conditions through to reconstruction. The simulations are not an 100% accurate representation of the POA array so that will introduce some differences too.

## 4.3 Resolution and Bias

To further evaluate the effects of increasing the NSB on the quality of the reconstructed EAS data, I look at the resolution and bias of both the reconstructed energy and reconstructed Xmax. A quick reminder that Xmax is the measurement of the brightest part of the shower relating to the maximum number of particles produced. For the smearing method the energy and Xmax bias is comparing to the measured data taken at standard NSB levels to the reconstructed with the increased NSB levels. For the simulations the energy and Xmax bias can be calculated using the true energy and Xmax values used to generate each EAS profile.

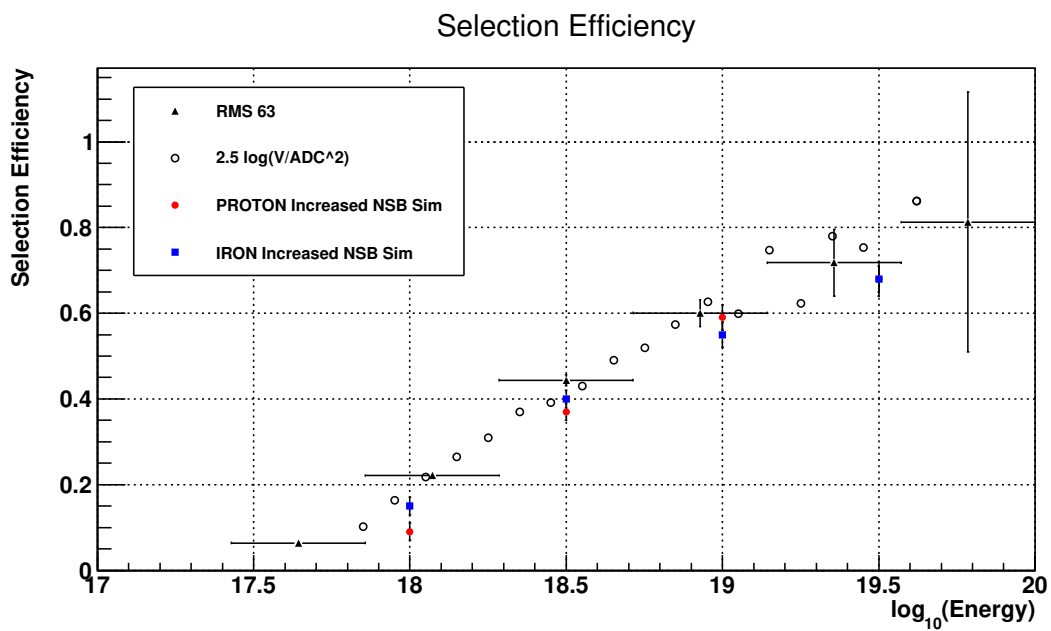


**Figure 4.1:** Selection Efficiency plot containing data from both the Smearing method and simulated showers. These results are compared to the work done by M. Unger.

The trend of the energy resolution for both methods is that as the energy of the EAS event increases the bias decreases. This was expected as the energy of the shower increases the brighter and longer the track that is observed. A brighter and longer track allows for a better reconstruction.

- Need to find out what's a good bias value for energy and Xmax.  
the energy and Xmax bias is calculated via:

$$\Delta E = \frac{E_{\text{recon}} - E_{\text{true}}}{E_{\text{true}}} \quad (4.7)$$

$$\Delta E = \frac{E_{\text{IncreasedNSB}} - E_{\text{StandardNSB}}}{E_{\text{StandardNSB}}} \quad (4.8)$$

$$\Delta X_{\text{max}} = X_{\text{max,rec}} - X_{\text{max,true}} \quad (4.9)$$

$$\Delta X_{\text{max}} = X_{\text{max,IncreasedNSB}} - X_{\text{max,StandardNSB}} \quad (4.10)$$

Eq. 4.7 and Eq. 4.9 are used on the simulated data sets while Eq. 4.8 and Eq. 4.10 is used on the smeared data set.

The energy and Xmax resolution is calculated via:

$$\sigma_{\text{res}} = \left( \frac{1}{N} \sum \frac{1}{\sigma_i^2} \right)^{1/2} \quad (4.11)$$

### 4.3.1 Comparing Simulated Data to Real Data

**Think about where to locate this section.**

Comparing the simulated data with real data. Checking to make sure that the simulation data is a good representation of reality. Looking at the Xmax distribution there is no need for a direction comparison as I only simulated proton and iron primaries and was not concern with have a particular mixtures. The other parameter I checked was the zenith angle distribution, distance to Xmax and distance to the shower axis ( $R_P$ ). The simulated profiles have similar shapes when both histograms are normalised to area of 1. For zenith angle distribution I simulated the EAS events upto a zenith angle of 60° so that the reason for the cut-off in the simulated data.

## 4.4 EAS Track Length in the FD's

One other parameter that was investigate was the shower track length observed by the FD's. It was expected that as the NSB increased the average observed shower track length would decrease. For both the smearing and simulation this trend was observed by not in a significant way. This is shown in Fig. 4.12 and Fig. 4.13. There was a thought about trying to extended track length into the noisy pixels as it would be known that would be photons observed at the start and end of the track. The measured data shows that this is not needed as not much of the track is lost with increased NSB. Especially at the highest energy bins where the most interest lays.

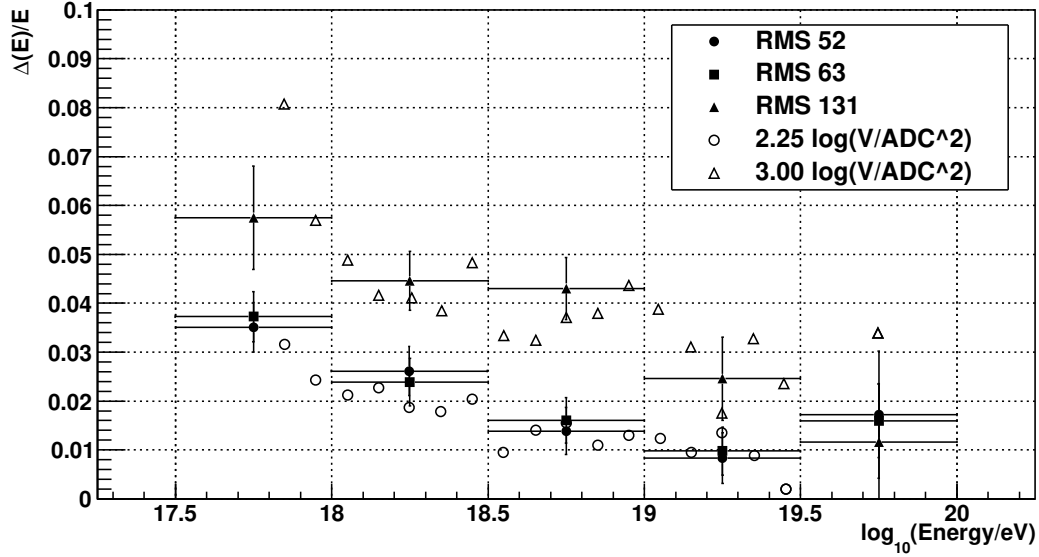


Figure 4.2: Energy Bias using Smearing Method.

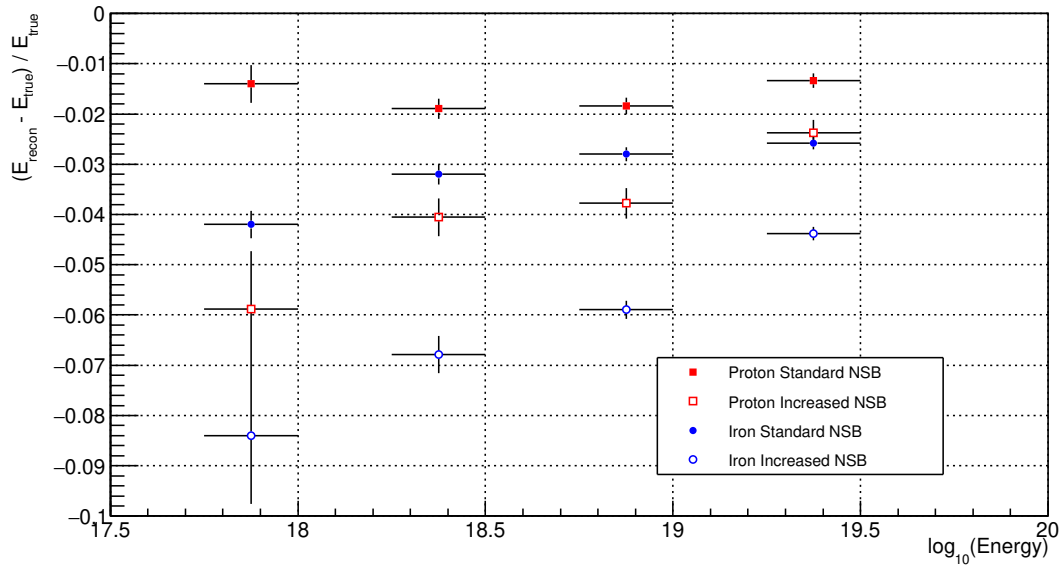
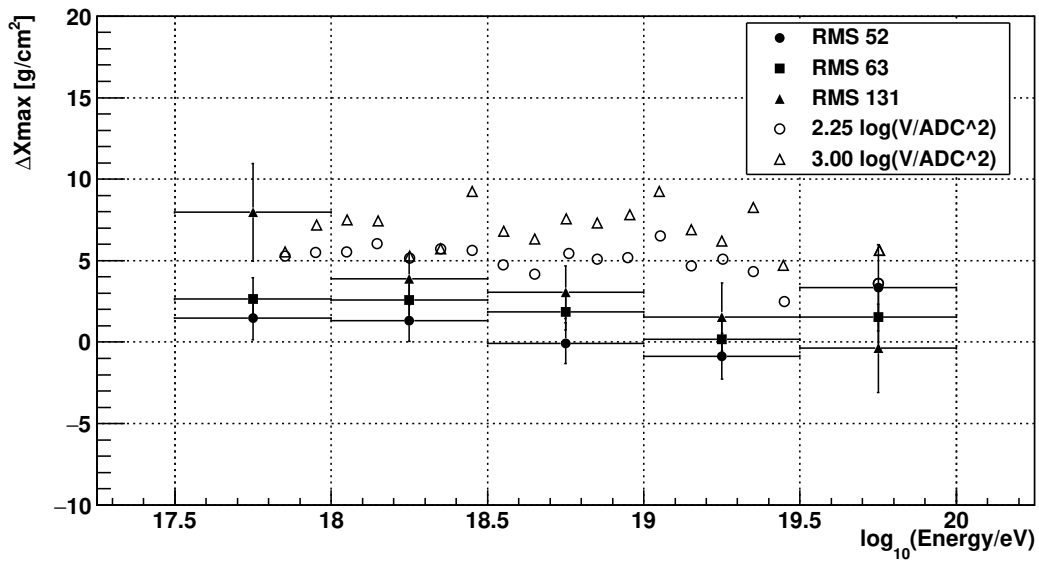
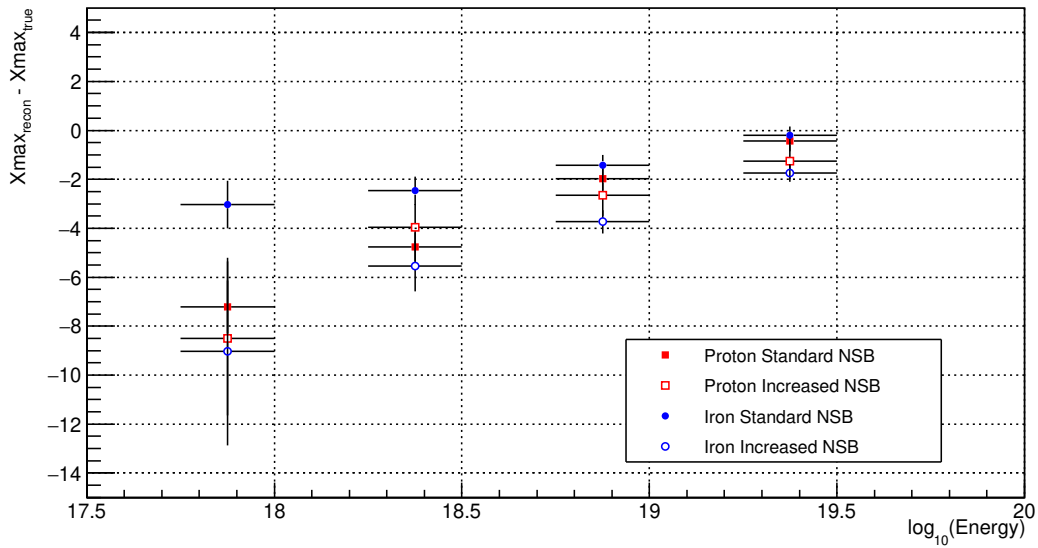


Figure 4.3: Energy Bias using simulated data.



**Figure 4.4:** Xmax Bias using Smearing Method.



**Figure 4.5:** Xmax Bias using simulated data.

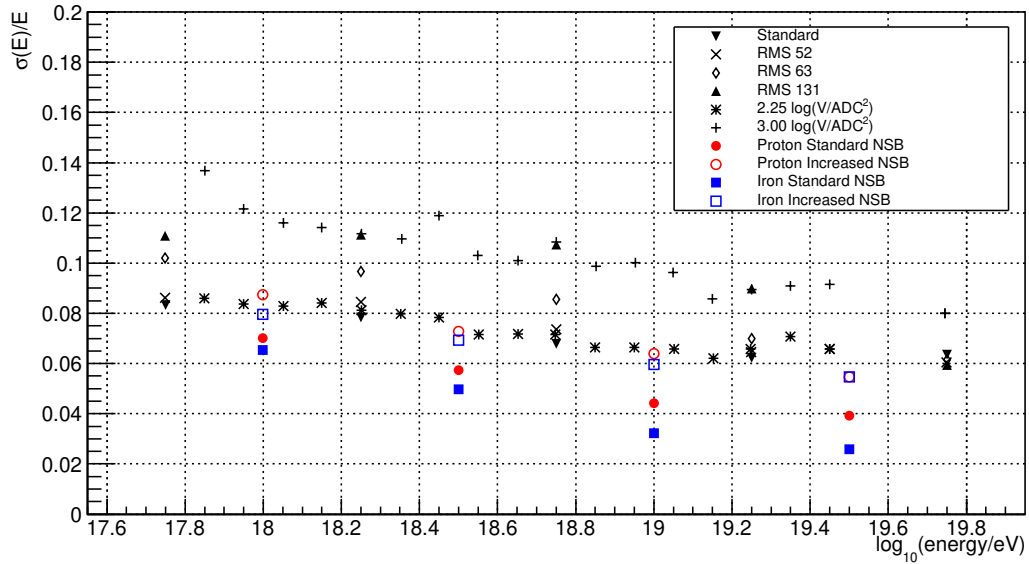


**Figure 4.6:** Energy Resolution using both Smearing Method data and simulated showers.

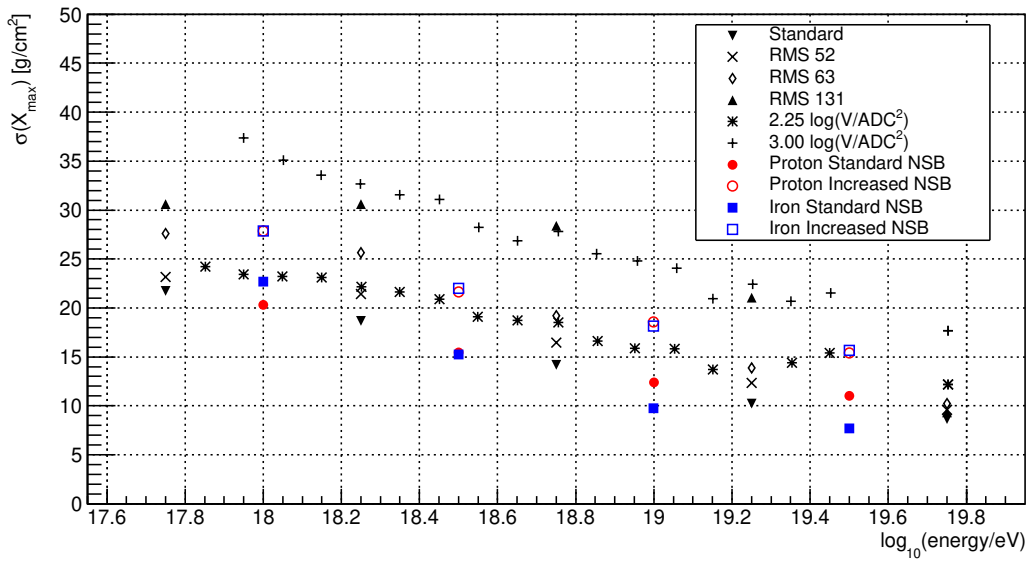


**Figure 4.7:** Xmax Resolution using both Smearing Method data and simulated showers.

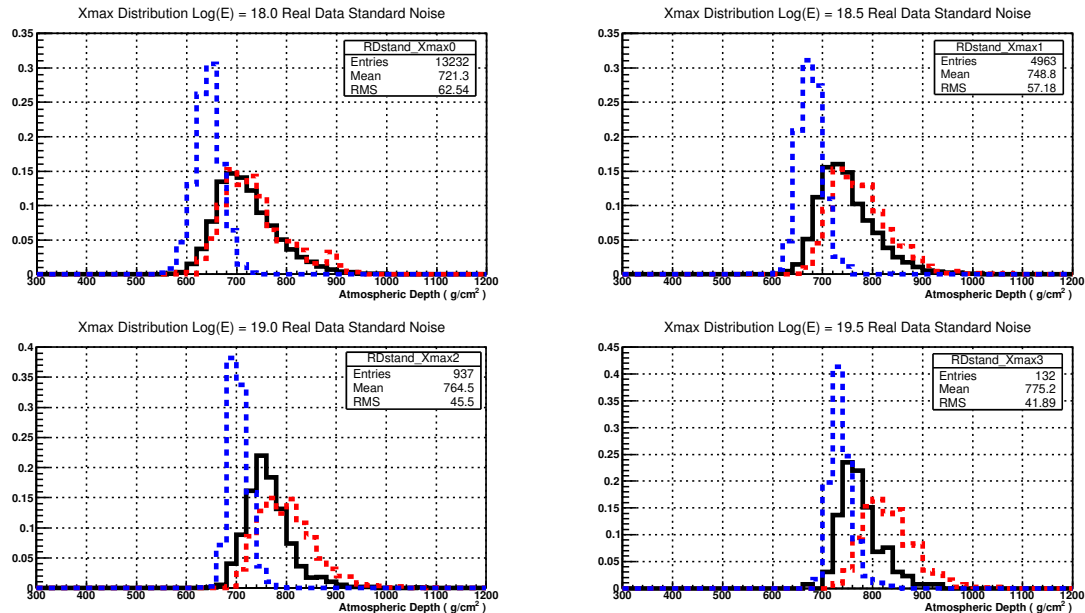


**Figure 4.8:** Distribution of Xmax with Real Data and simulation of proton and iron showers.

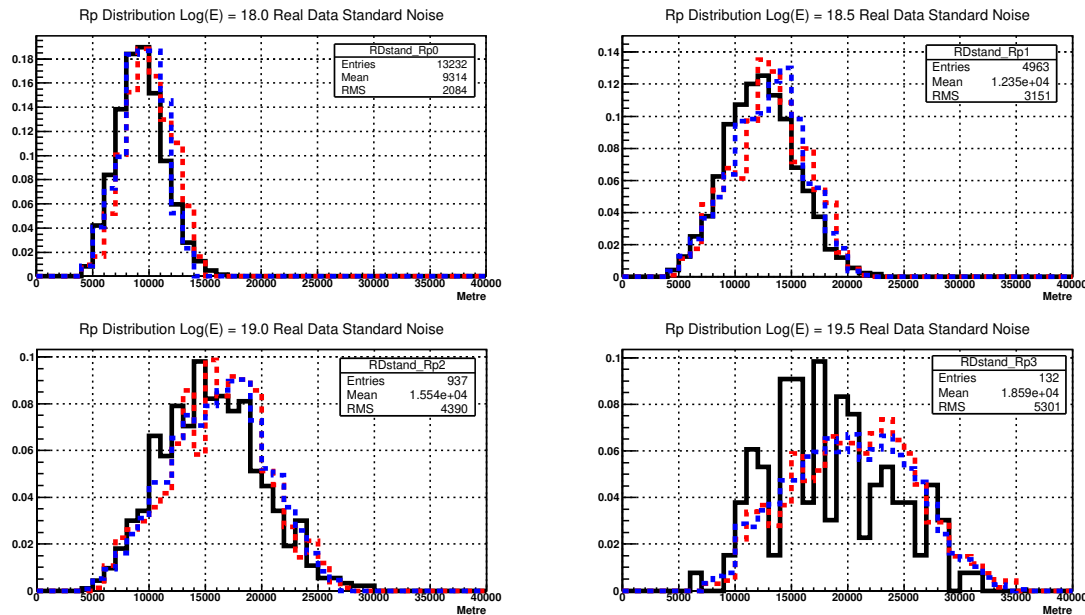


**Figure 4.9:** Distribution of Rp with Real Data and simulation of proton and iron showers.

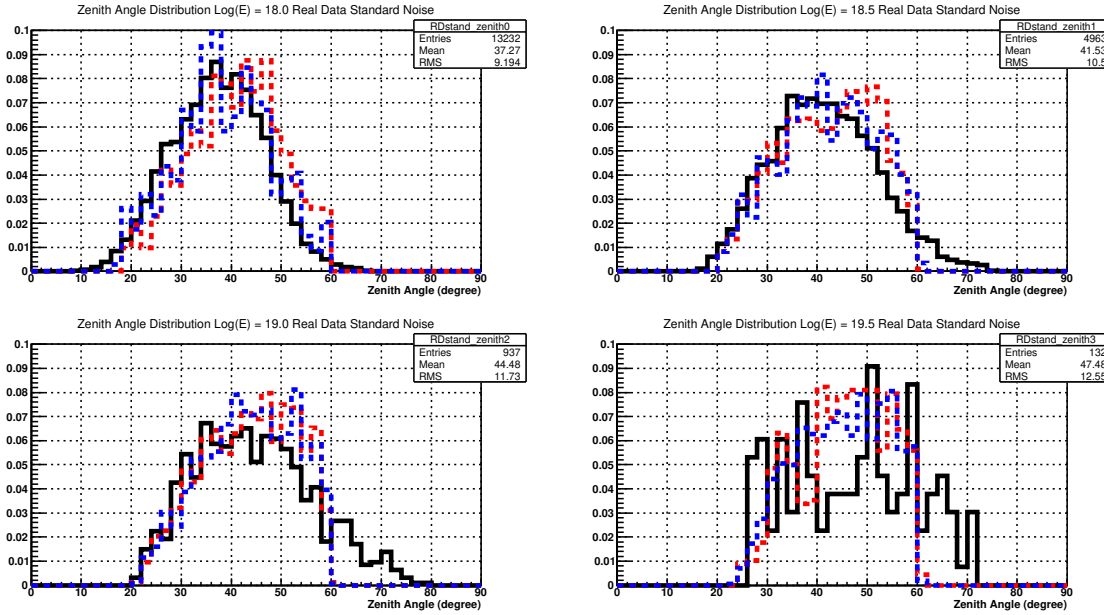


**Figure 4.10:** Distribution of Zenith angle with Real Data and simulation of proton and iron showers.

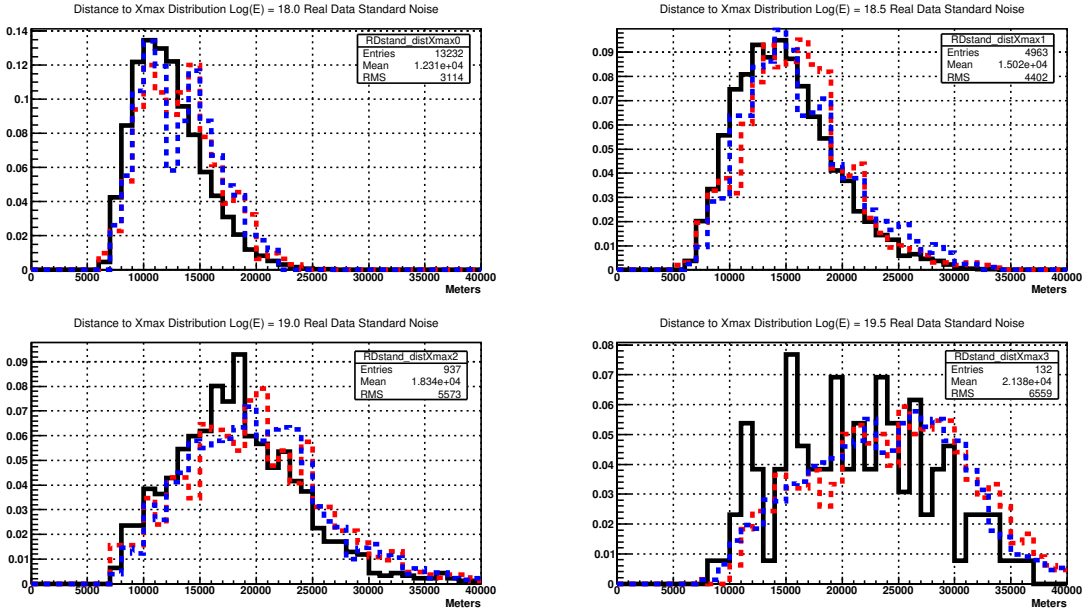


**Figure 4.11:** Distribution of Distance to Xmax with Real Data and simulation of proton and iron showers.

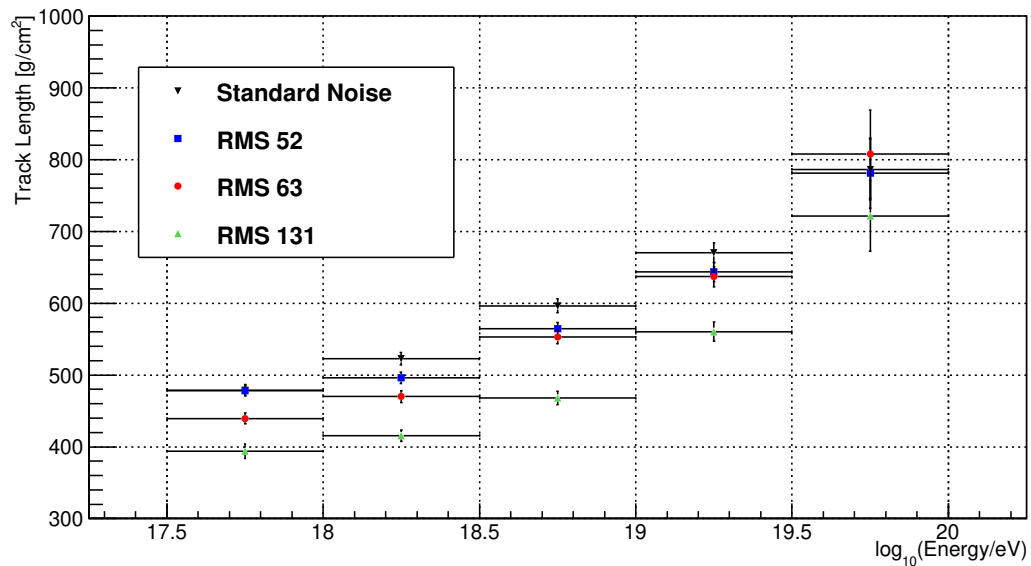


**Figure 4.12:** Track length using Smearing method.

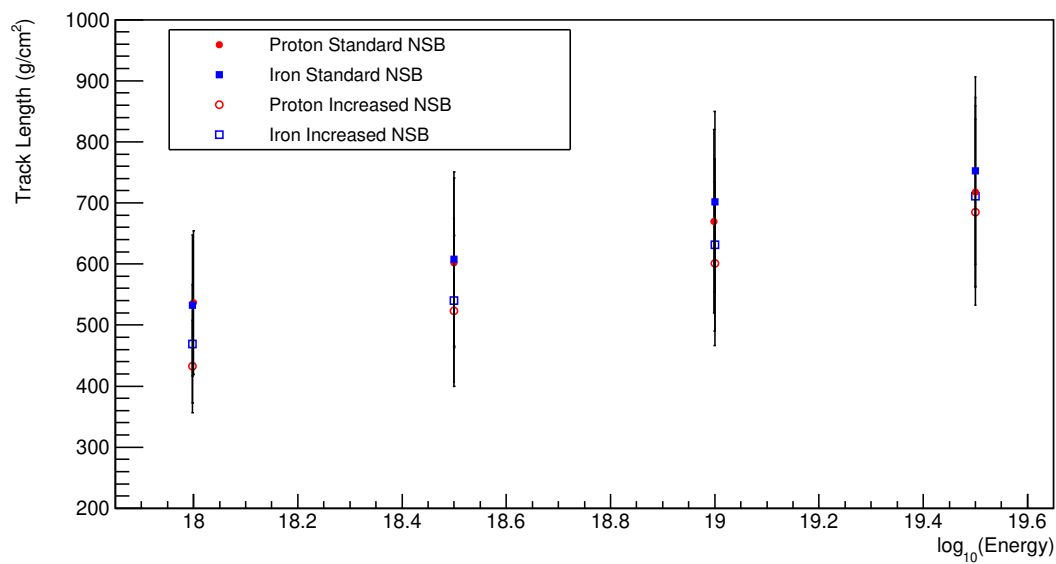


**Figure 4.13:** Track length using simulation of proton and iron CONEX showers.



# Chapter 5

## Quantifying Characteristics of the FD PMT

Characterising the PMT at 600V and 900V

- Using the characteristics of the PMT at 900V as a baseline
- Measure linearity
- ND filters vs Two LED method
- temperature effects

Measuring the PMT characteristics at both 900V and 600V. The aim is to use the measurements done at 900V as the baseline of expected performance and then observe the repeated measurements at 600V. We have a good understanding of the characteristics of the PMT operating at 900V due to this being the nominal voltage that the PMTs in the FD telescopes are run at. I explore the characteristics at 600V as we are expecting to reduce the PMT gain by a factor of 10 and this related to an approximate voltage drop to 600V. This may be an over estimate but we can be confident if the PMT voltage used is greater than 600V then the characteristics will be the same.

### 5.1 PMT Linearity

One of the main characteristics of a Photomultiplier Tube (PMT) to measure is its linearity. A PMT linearity is where if a light intensity is doubled the PMT response doubles as well. It is important to quantify this region to be confident that if the light intensity changes the PMT response follows.

I look at two methods to measure the PMT linearity - using Neutral Density filters and the Two LED method.

#### 5.1.1 Neutral Density Filters

The method of using Neutral Density filters involves employing filters to reduce the light intensity reaching the PMT cathode by a known amount. The filters were used singularly and in combination to get different Optical Transmission. The filters are

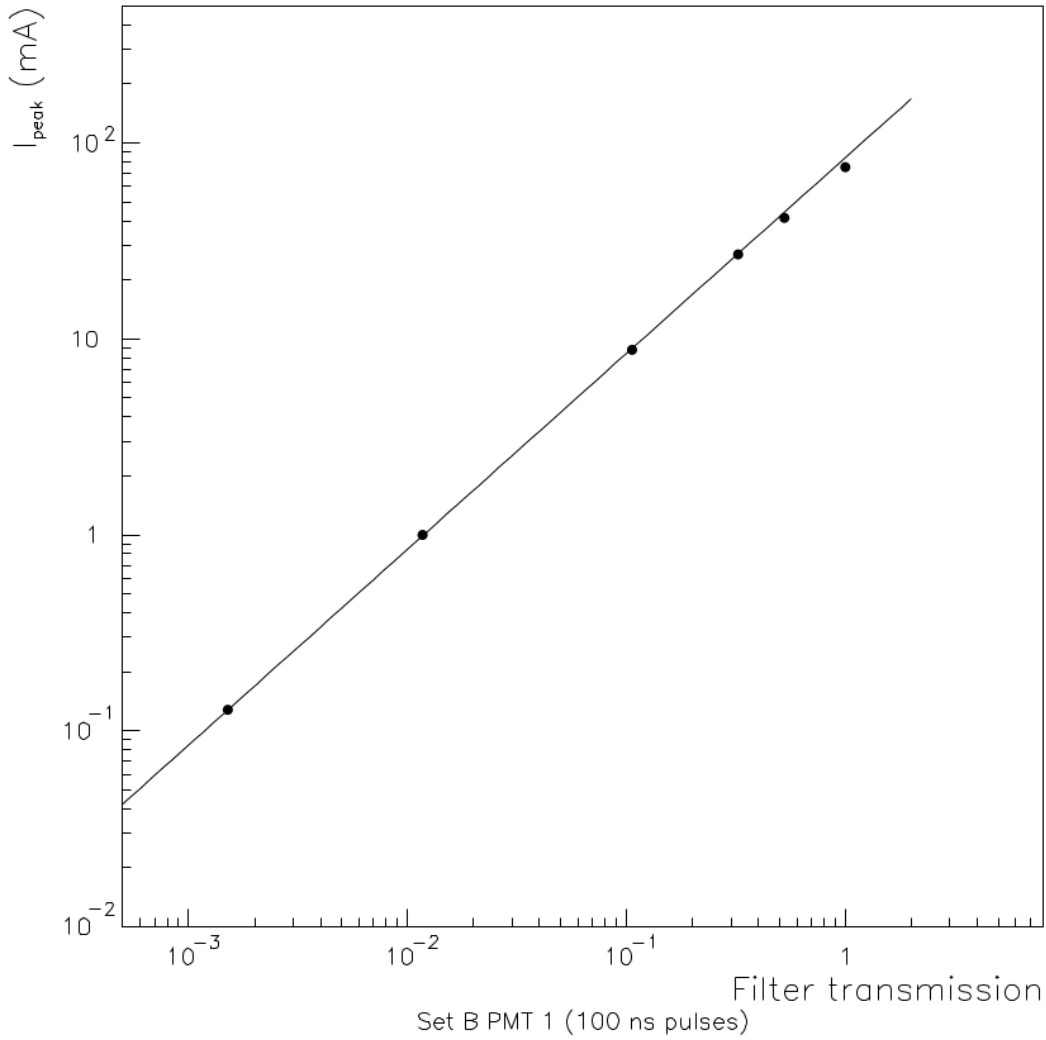


**Figure 5.1:** Previous PMT linearity test done by Privitera et. al. 1999 with Neutral density filters.

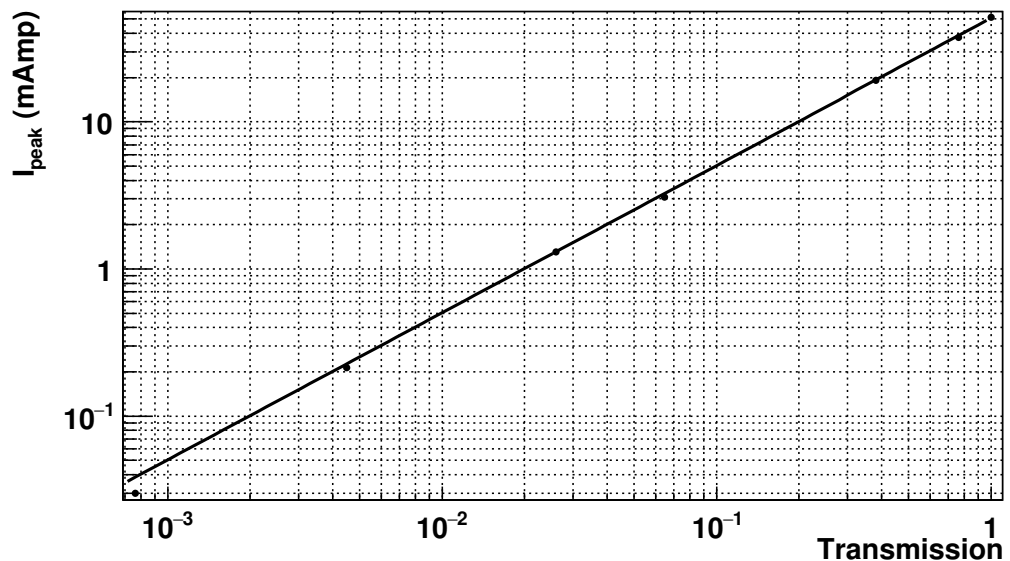
label with optical density which is different to optical depth. To convert optical density to transmission:

$$\text{Optical Depth} = -\log_{10} \left( \frac{\text{Transmission}}{100} \right) \quad (5.1)$$

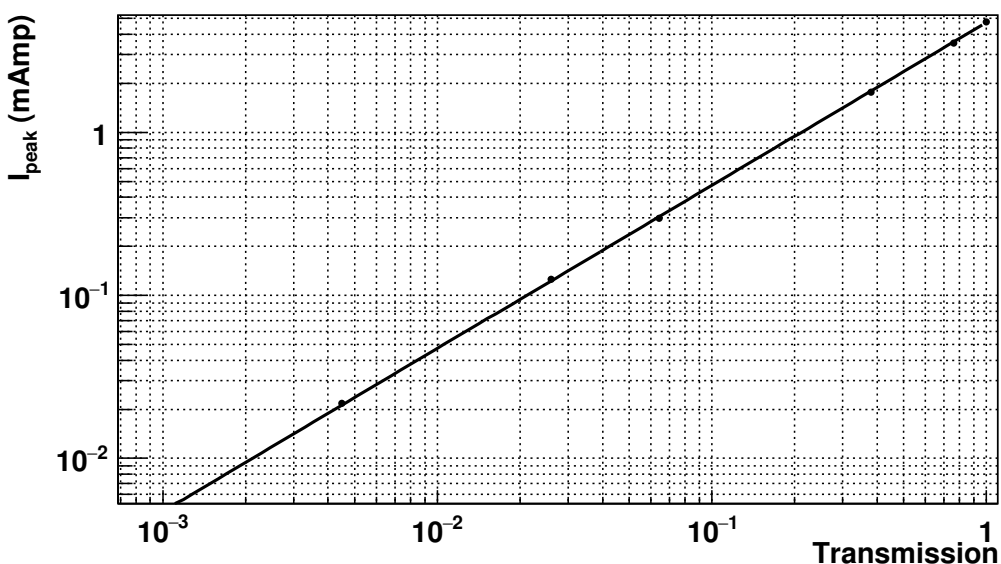
To get different transmission values, the filters can be stack and the optical depth values just add together (IE. if using two filters one with ND 0.4 and ND 0.1 the total ND will be 0.5).

I repeated a study done by Privitera et. al. (1990) ref. on Auger PMTs. I wanted to use the result done at an High Voltage value of 900V as my baseline then continue the study to observe the result at an High Voltage value of 600V.

Some of the disadvantages of using Neutral Density filters it that you are restricted to fixed units of transmission depending on which filters you have access too. Also you are relying on the fact that the optical density doesn't change over time and is not effected by handing and storage. There is also some uncertainty on the optical density value quote.



(a)



(b)

**Figure 5.2:** Neutral density method at 900V and 600V.

### 5.1.2 Two LED Method

Another method investigate was the two LED method. This method was first used in the original measurement of the SD PMTs ref. To measure the linearity, two LEDs are pointed at the PMT and with one set of observations taken with the LEDs on separately then one set taken with the LEDs on at the same time. A graphical representation is shown in Fig. 5.3 of the set-up used to measure the PMT linearity at both 900V and 600V. Two pulse generators are used to drive the LEDs separately and to allow the two pulses to overlap when needed to measure the PMT response to the LEDs on at the same time. To find the linearity a ratio is plotted against peak pulse ampere. the ratio is calculated via:

$$\text{Ratio} = \frac{\text{LED}_{1+2}}{\text{LED}_1 + \text{LED}_2} \quad (5.2)$$

where  $\text{LED}_{1+2}$  is the measurement when both LEDs are on at the same time, and  $\text{LED}_1$  and  $\text{LED}_2$  is the measurement when they are on separately. The principle employed here is that while the intensity is within the linearity region the peak of  $\text{LED}_{1+2}$  should equal the addition of  $\text{LED}_1$  and  $\text{LED}_2$  separately. Therefore the ratio should be one while both peak anode ampere from the LEDs on separately and LEDs on together are within the region of linearity. As the light intensity is increased the LEDs on together will first move out of the region of linearity first. Typically this means that the peak ampere measured from both LEDs on at the same time will be less than the combination of the peak ampere when measured separately. This will cause the ratio to dip below one.

The advantages of this method is that any LED levels can be used and do not have to worry about the two LEDs linearity. As long as the two LED intensities are different it will produce a different response in the PMT.

The result of the two LED Method is shown in Fig. 5.4 for both 900V and 600V. The x-axis is the peak ampere of the measured pulses when both LEDs are on at the same time. The plots show that while the peak anode currents change by a close factor of 10, the gain of the PMT has also been reduced by a similar factor. This seems to indicate that the cathode is the limiting factor for the PMT linearity for this type. **Maybe quote theoretical peak anode current for a  $10^{21}$  eV shower.**

## 5.2 Effects of Temperature on PMT Gain

Quoted on any PMT data sheet is the expected change in gain as a function of energy. The XP3062 PMT used in the FD telescopes is quoted to be  $-0.2\%/\text{K}$ . I measured this value in the lab at University of Adelaide at both 900V and 600V. The set-up to monitor the gain of the PMT involved a LED inside a copper oven pointed at the cathode pulsed once per second, and a temperature gauge. I was able to control the laboratory temperature to see the gain change over a variety of temperature values. The LED was inside a copper oven to maintain an independent constant temperature so the number of photons emitted could be considered to be fixed. The PMT was inside a box that highly light proof - the top was held down with screws, then two layers of black electrical tape was applied to the lid joinings and then a black out curtain was draped over the top. Only the temperature was allowed to vary over the measurement period. Therefore any changes in the absolute ADC measurements are related to changes in the PMT gain.

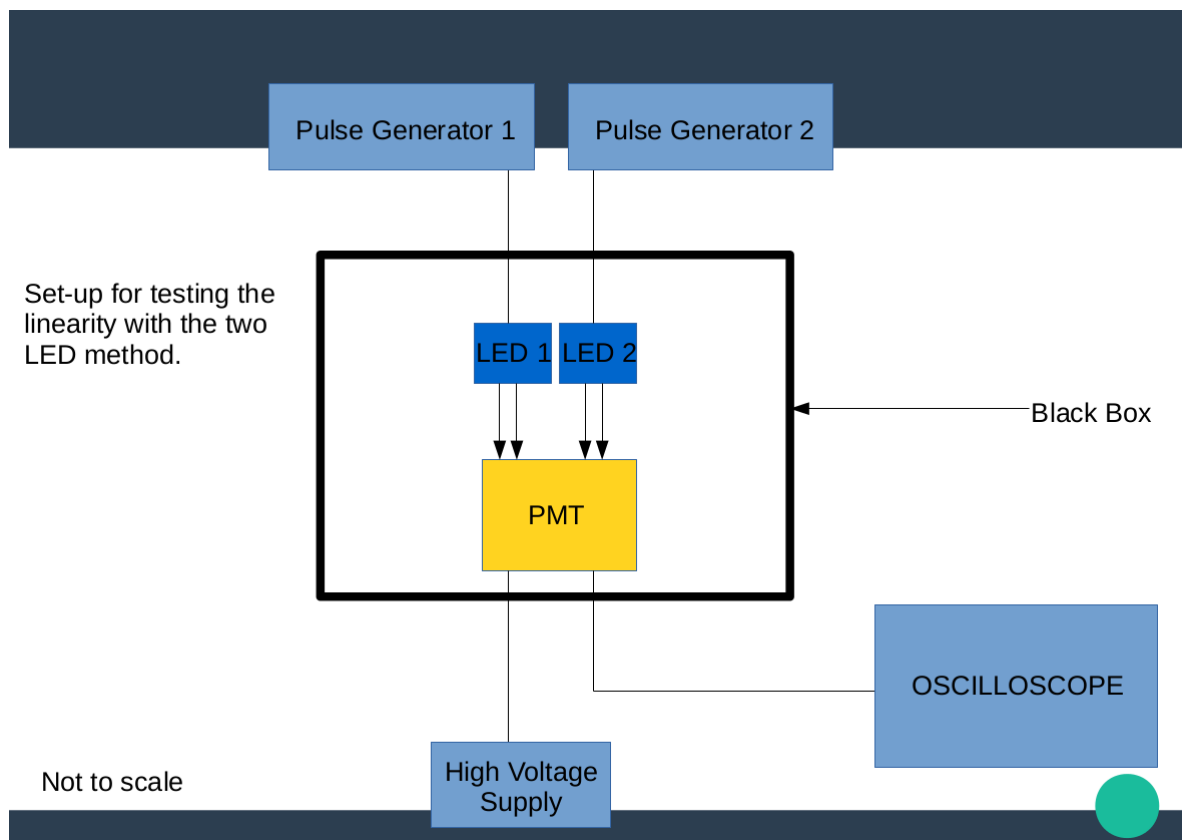


**Figure 5.3:** A graphical representation of the Two LED Setup used in the lab at University of Adelaide.

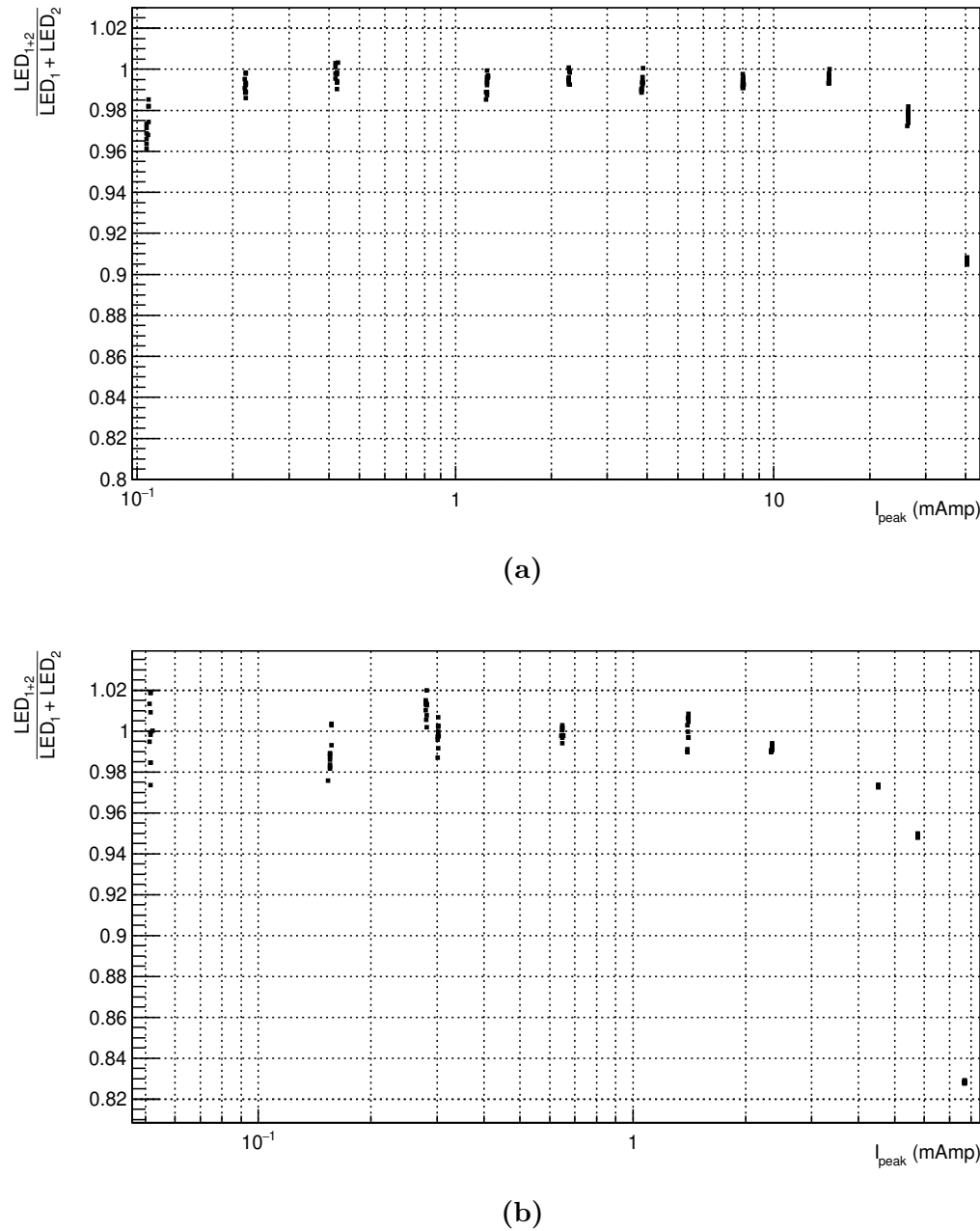
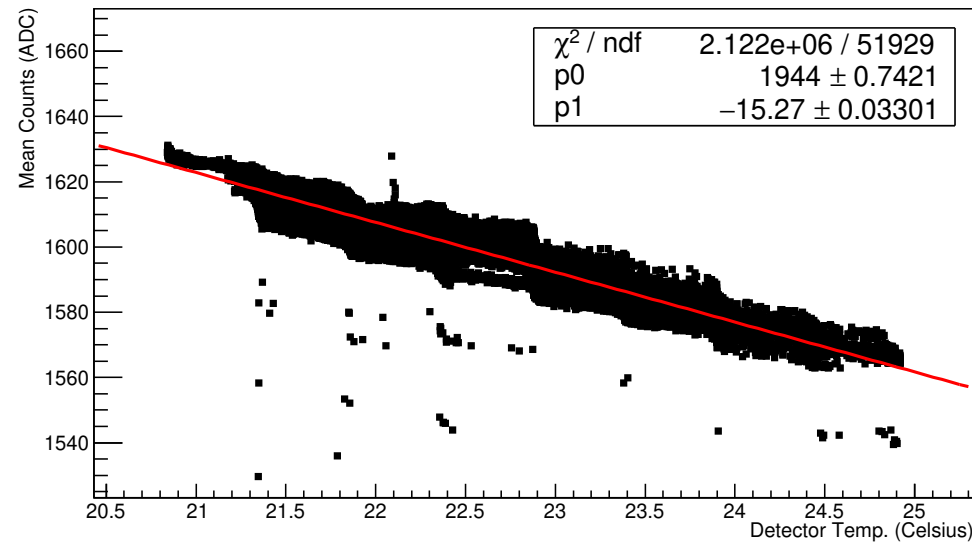
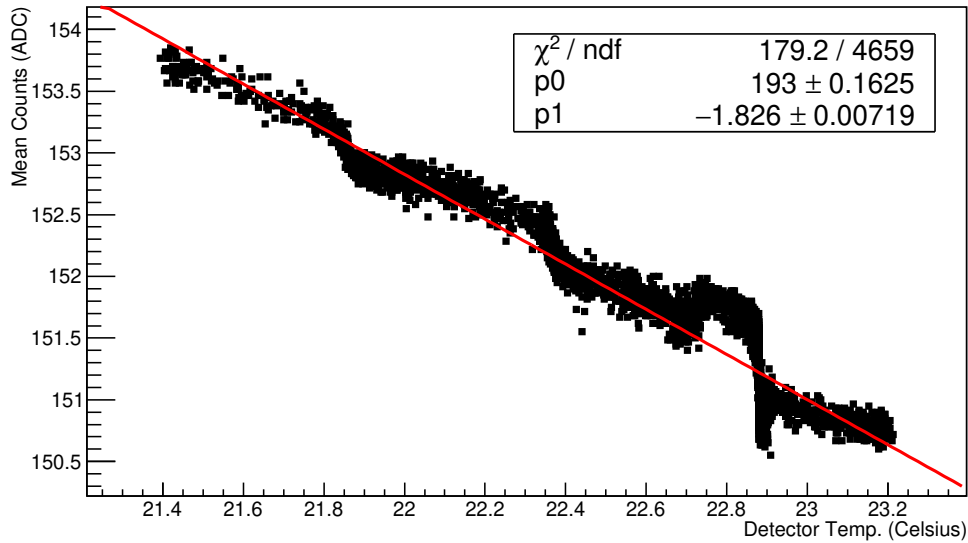


**Figure 5.4:** Two LED method at 900V and 600V.

Measurements for temperature vs PMT gain was taken at both High Voltage values of 900V and 600V. The plots in Fig. 5.5 the effects of temperature on the PMT can be clearly seen at both high voltage values. For either high voltage value the measured PMT gain change per K was  $-0.6\%\text{K}$  needs uncertainty. This maybe different to the quoted data sheet but is not unreasonable. The quoted data sheet is an average of many PMTs while this is a measurement of one particular PMT. What was interested was that this value did not deviate if using the PMT at 900V or 600V.



(a)



(b)

**Figure 5.5:** Showing the how PMT gain correlates with surrounding temperature.

# Chapter 6

## Computer Simulation of FD PMT

Simulating the FD PMT under differing NSB and for different reasons.

- Theoretical value for Gain Variance
- PMT Gain Variance
- Show both for flat distribution and Gaussian variations for dynodes
- Results
- FD FLT under increased NSB

### 6.1 Method and Theory

To get a deeper understanding of how a PMT gain variance I used a toy model Monte Carlo to follow simulated electrons throughout the PMT chain. Gain Variance is the Gaussian broadening of the measured anode signal. The number of electrons that are emitted off of each dynode follows a Poisson distribution but as electrons travel further down the dynode chain and the number of electrons emitted per dynode increase the distribution becomes more Gaussian like. When an electron hits a dynode there is a probability distribution that is Poission in shape. As the number of electrons hitting an individual dynode increases the overlapping Poission distribution becomes more Gaussian in shape.

To simulate the Gain Variance within a PMT I set-up 8 dynode stages to match the XP3062 PMT used by the FD telescopes. I was only looking at the single photo-electron case (IE. where only a single electron is emitted from the cathode.). If there was no extra broadening then the distribution would be dictated by the Poisson distribution. For each electron that hits a dynode a random number generator is used to determine the number of electrons that leave the dynode.

**Draw flow chart of toy model Monte Carlo.**

#### 6.1.1 Theoretical value of Gain Variance?

Investigated different scenarios - each dynode able to emit uniformly across its surface and each dynode having some sort of irregularity across its surface. The irregularity was added by shifting the mean of the Poisson distribution by sampling from a random Gaussian distribution. The gain variance was investigated at different PMT gain values.

The PMT gain values was equivalent to a high voltage across the PMT of 1300V, 900V and 600V. 1300V was picked as that the high voltage for which a gain variance measurement was preformed by Auger, 900V is the typical high voltage used when running the FD telescopes and 600V is the approximate high voltage to be used when using the FD telescopes to observe under increased NSB conditions.

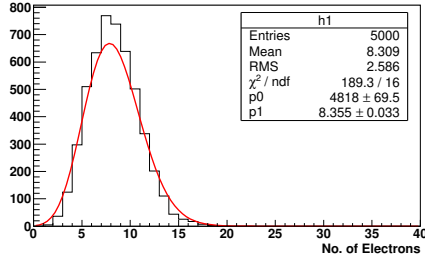
## 6.2 Results of PMT Gain Variance Simulation

### 6.3 Simulation of Gain Variance Method

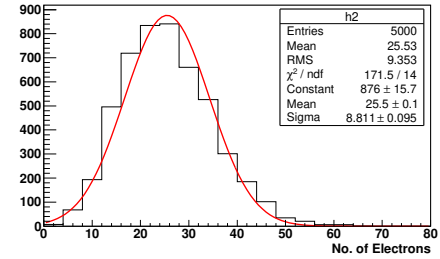
- Show off histogram of simulated Gain Variance Ratios
- Show that there's a natural spread
- some of the calculated ratio's will be less then one due to spread in measure variances
- differences in methods? Pairs vs averages method should return the same results
- benefits of combining noise traces over using just 140 bins per trace.

### 6.4 FD FLT under different NSB levels

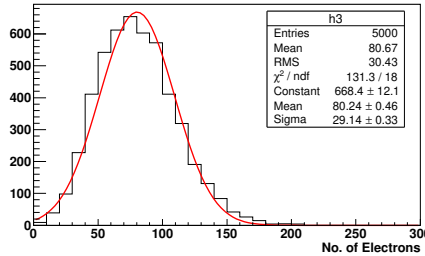
Looked at study to simulate the effects of increased NSB on the First Level Trigger (FLT). The PAO maintains the FLT to trigger at 100 Hz range. From simulations with different NSB levels it can be seen trigger threshold above the mean would be required to maintain the expected trigger level. The NSB of  $2.71 \setminus 100$  ns is the typical NSB level observed at the site. From there I picked 5 increased NSB levels to show how threshold above the mean changes.



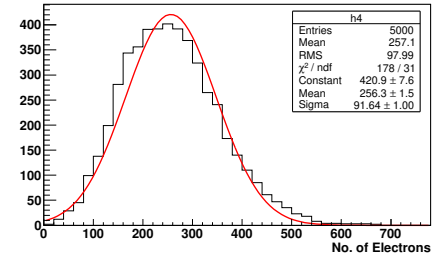
(a) Distribution of simulated electrons leaving dynode 1. The red line is a fitted Poisson distribution.



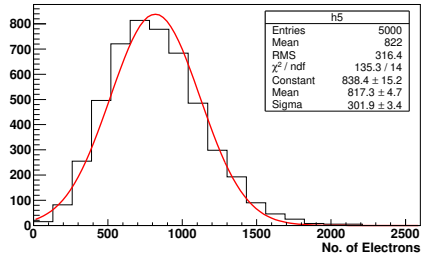
(b) Distribution of simulated electrons leaving dynode 2. The red line is a fitted Gaussian distribution.



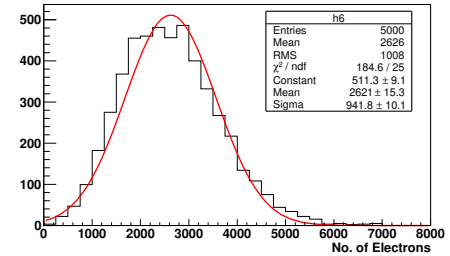
(c) Distribution of simulated electrons leaving dynode 3. The red line is a fitted Poisson distribution.



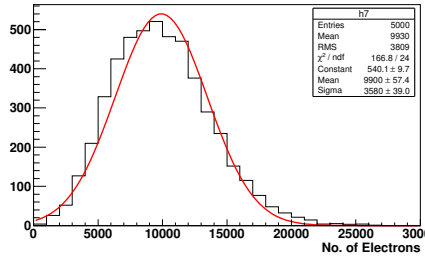
(d) Distribution of simulated electrons leaving dynode 4. The red line is a fitted Gaussian distribution.



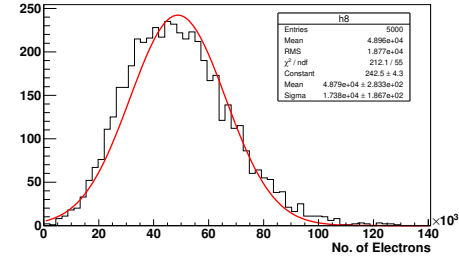
(e) Distribution of simulated electrons leaving dynode 5. The red line is a fitted Poisson distribution.



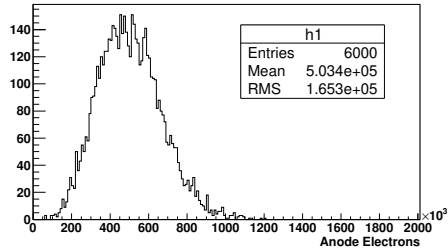
(f) Distribution of simulated electrons leaving dynode 6. The red line is a fitted Gaussian distribution.



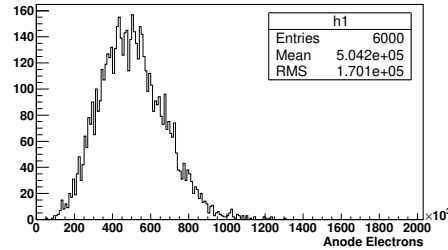
(g) Distribution of simulated electrons leaving dynode 7. The red line is a fitted Poisson distribution.



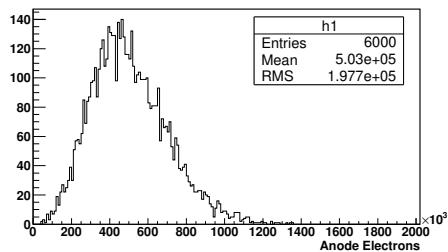
(h) Distribution of simulated electrons leaving dynode 8. The red line is a fitted Gaussian distribution.



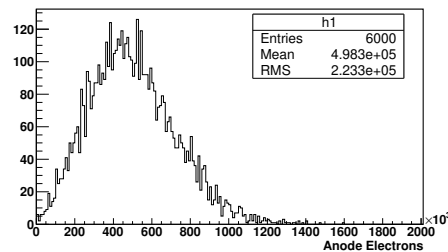
(a) Simulated observed signal from PMT anode with 8 stages and gain of  $5 \times 10^5$ . Poisson fluctuations at each stage only. No each Gaussian broadening at any dynode.



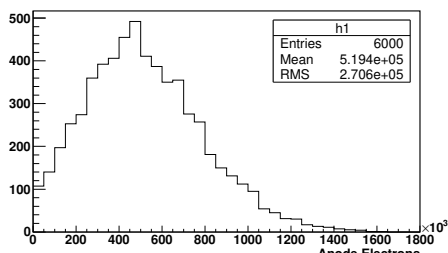
(b) Simulated observed signal from PMT anode with 8 stages and gain of  $5 \times 10^5$ . Poisson fluctuations at each stage only. Added Gaussian broadening at each dynode of 10%.



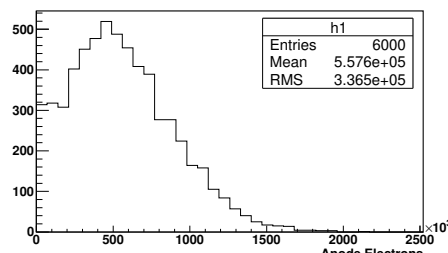
(c) Simulated observed signal from PMT anode with 8 stages and gain of  $5 \times 10^5$ . Poisson fluctuations at each stage only. Added Gaussian broadening at each dynode of 20%.



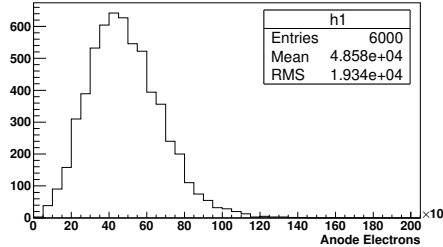
(d) Simulated observed signal from PMT anode with 8 stages and gain of  $5 \times 10^5$ . Poisson fluctuations at each stage only. Added Gaussian broadening at each dynode of 30%.



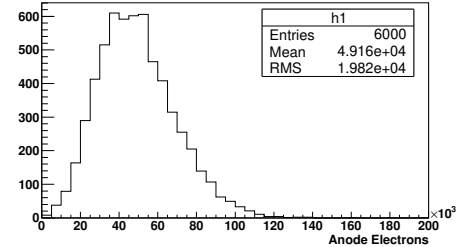
(e) Simulated observed signal from PMT anode with 8 stages and gain of  $5 \times 10^5$ . Poisson fluctuations at each stage only. Added Gaussian broadening at each dynode of 40%.



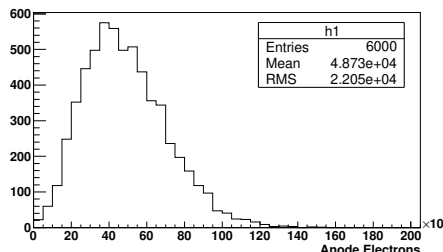
(f) Simulated observed signal from PMT anode with 8 stages and gain of  $5 \times 10^5$ . Poisson fluctuations at each stage only. Added Gaussian broadening at each dynode of 50%.



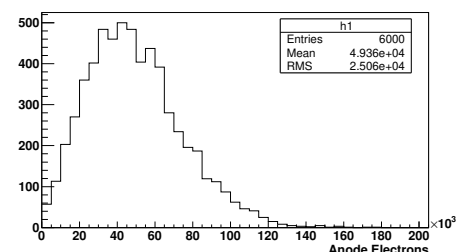
(a) Simulated observed signal from PMT anode with 8 stages and gain of  $5 \times 10^4$ . Poisson fluctuations at each stage only. No each Gaussian broadening at any dynode.



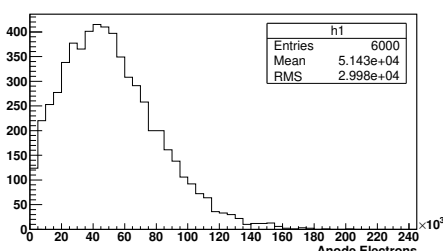
(b) Simulated observed signal from PMT anode with 8 stages and gain of  $5 \times 10^4$ . Poisson fluctuations at each stage only. Added Gaussian broadening at each dynode of 10%.



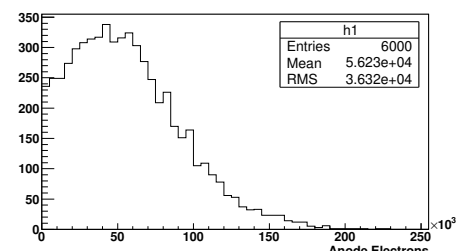
(c) Simulated observed signal from PMT anode with 8 stages and gain of  $5 \times 10^4$ . Poisson fluctuations at each stage only. Added Gaussian broadening at each dynode of 20%.



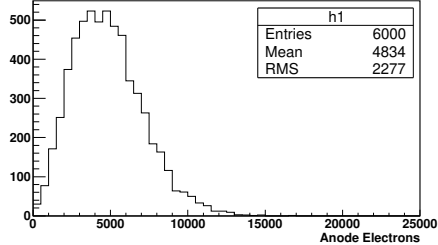
(d) Simulated observed signal from PMT anode with 8 stages and gain of  $5 \times 10^4$ . Poisson fluctuations at each stage only. Added Gaussian broadening at each dynode of 30%.



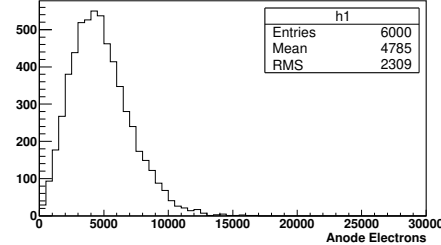
(e) Simulated observed signal from PMT anode with 8 stages and gain of  $5 \times 10^4$ . Poisson fluctuations at each stage only. Added Gaussian broadening at each dynode of 40%.



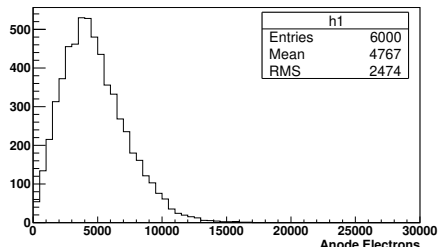
(f) Simulated observed signal from PMT anode with 8 stages and gain of  $5 \times 10^4$ . Poisson fluctuations at each stage only. Added Gaussian broadening at each dynode of 50%.



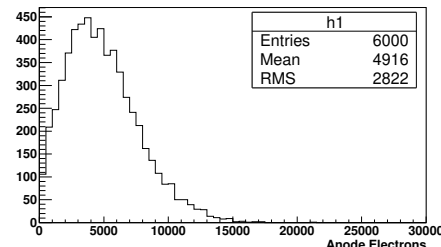
(a) Simulated observed signal from PMT anode with 8 stages and gain of  $5 \times 10^3$ . Poisson fluctuations at each stage only. No each Gaussian broadening at any dynode.



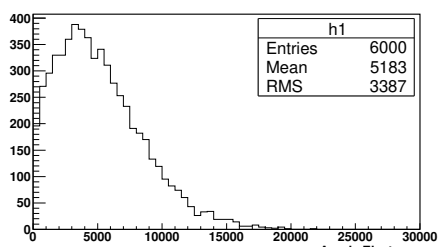
(b) Simulated observed signal from PMT anode with 8 stages and gain of  $5 \times 10^3$ . Poisson fluctuations at each stage only. Added Gaussian broadening at each dynode of 10%.



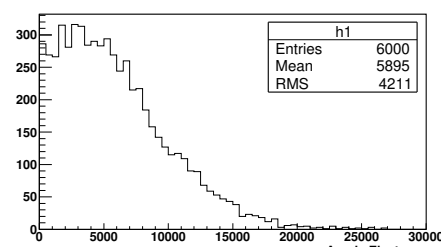
(c) Simulated observed signal from PMT anode with 8 stages and gain of  $5 \times 10^3$ . Poisson fluctuations at each stage only. Added Gaussian broadening at each dynode of 20%.



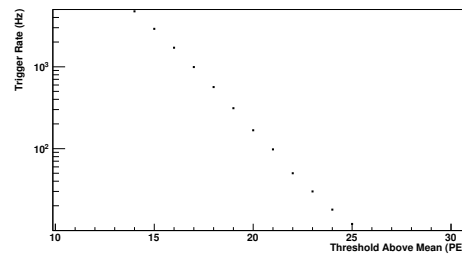
(d) Simulated observed signal from PMT anode with 8 stages and gain of  $5 \times 10^3$ . Poisson fluctuations at each stage only. Added Gaussian broadening at each dynode of 30%.



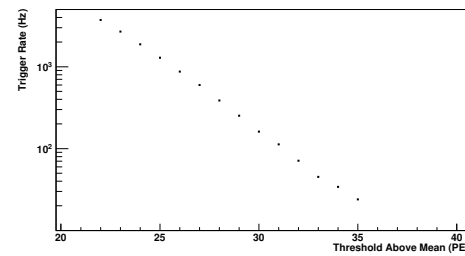
(e) Simulated observed signal from PMT anode with 8 stages and gain of  $5 \times 10^3$ . Poisson fluctuations at each stage only. Added Gaussian broadening at each dynode of 40%.



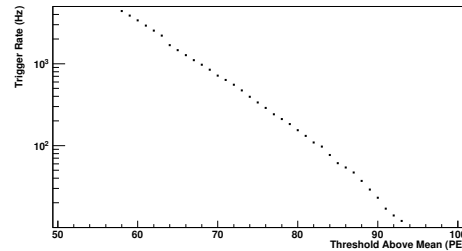
(f) Simulated observed signal from PMT anode with 8 stages and gain of  $5 \times 10^3$ . Poisson fluctuations at each stage only. Added Gaussian broadening at each dynode of 50%.



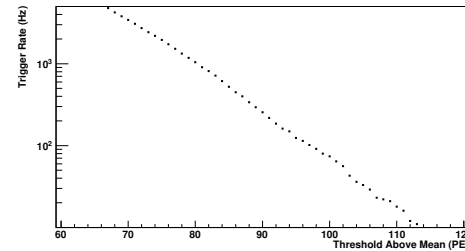
(a) FLT simulation with NSB of 2.71 pe / 100ns.



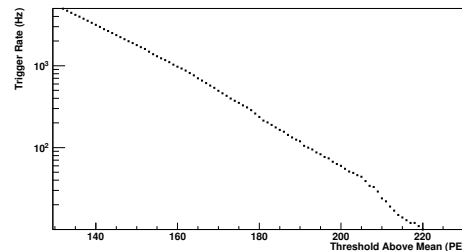
(b) FLT simulation with NSB of 6.60 pe / 100ns.



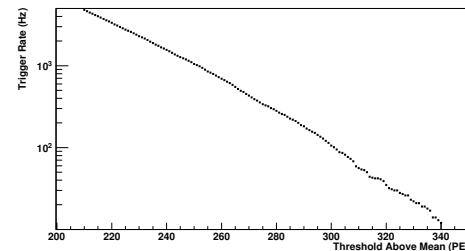
(c) FLT simulation with NSB of 46.8 pe / 100ns.



(d) FLT simulation with NSB of 65.8 pe / 100ns.



(e) FLT simulation with NSB of 263 pe / 100ns.



(f) FLT simulation with NSB of 657 pe / 100ns.



# Chapter 7

## Measuring FD PMT Gain Variance with CalA Data

Measuring Gain Variance of FD PMT with CalA Data

- Measuring Gain Variance in the lab did not work. Equipment was not sensitive enough to the low current.
- There was issues with calibrating the LED light source with another PMT (QE curve and wavelength response not the same?)
- Using Low/Standard measurements of CalA to find Gain Variance Ratio
- Two different methods
- Bootstrap method to find uncertainties on Method 2

### 7.1 Using CalA to measure relative changes in Gain Variance

Using CalA data from the FD telescopes to measure the relative changes in PMT gain variance as the gain is changed by a factor of 10. CalA data is calibration data used to monitor any changes in PMT gain as a function of time. CalA is performed at the beginning and end of a nightly observation done with the FDs. Pulses from a monitored light source are piped to point at the camera. There are 50 pulses sent with a width of approximately  $60 \mu\text{s}$ .

**show image of CalA pulse**

One of the values that can be calculated from the CalA is a value denoted  $K_V$ .  $K_V$  is calculated via:

$$K_V = \frac{\text{Mean}}{\text{Sigma}^2} = \frac{10}{2 \times G(1 + V_G) \times F} \quad (7.1)$$

Mean is the average ADC count of the observed CalA pulse seen the FD pixel, sigma<sup>2</sup> is the variance calculated around fit to the signal in ADC<sup>2</sup>. The signal has a slope due to the effects of a capacitor used to remove the DC component of the signal. The slope is proportional to the time constant of the capacitor employed. G is the PMT gain, F is the noise equivalent bandwidth (Hz) and  $V_G$  is the PMT gain variance.

The absolute value of the gain variance cannot be found but using  $K_V$  a relative change can be found. This is useful for the collaboration simulations as a Gain variance

is coded for the PMT at standard voltage settings. Finding out the relative change in gain variance would be useful to be used for simulations of the FD PMTs at a lower voltage settings (IE. 600V).

The method used to measure the ratio in gain variance is to take the calculated means and sigmas from the pulses and then find a ratio between the  $K_V$  and Gains at the two different voltage settings.

$$K = \frac{\text{Mean}}{\text{Sigma}^2} = \frac{10}{2 \times G(1 + V_G) \times F} \quad (7.2)$$

$$\frac{(K_V)_{\text{Low}}}{(K_V)_{\text{Stand}}} = \frac{\text{Mean}_{\text{Low}}}{\text{Sigma}_{\text{Low}}^2} \div \frac{\text{Mean}_{\text{Stand}}}{\text{Sigma}_{\text{Stand}}^2} \quad (7.3)$$

$$\frac{\text{Mean}_{\text{Low}}}{\text{Sigma}_{\text{Low}}^2} \div \frac{\text{Mean}_{\text{Stand}}}{\text{Sigma}_{\text{Stand}}^2} = \frac{G_{\text{Stand}}(1 + V_G)_{\text{Stand}}}{G_{\text{Low}}(1 + V_G)_{\text{Low}}} \quad (7.4)$$

$$\frac{G_{\text{Stand}}}{G_{\text{Low}}} = \frac{\text{Mean}_{\text{Stand}}}{\text{Mean}_{\text{Low}}} \quad (7.5)$$

$$\frac{(1 + V_G)_{\text{Low}}}{(1 + V_G)_{\text{Stand}}} = \frac{\text{Sigma}_{\text{Low}}^2 \times \text{Mean}_{\text{Stand}}^2}{\text{Sigma}_{\text{Stand}}^2 \times \text{Mean}_{\text{Low}}^2} \quad (7.6)$$

## 7.2 Electronic Noise

Investigated the consistency of the electronic noise across a set of 50 CalA traces. The consistency was looked as there is only about 140 bins of noise before the signal pulse start. Therefore finding an accurate mean and variance of the electronic noise on an individual pulse is difficult. An accurate measurement of the electronic noise mean and variance was required as the measured gain variance ratio was only a few percent.

### Need to show electronic noise as function of time.

An example of a pixel electronic noise trace is shown in Fig. ???. It can be seen in this figure that stitching all of the noise bins from the 50 traces is remarkably stable. This result allows for all the noise for a single PMT pixel to be place into a histogram to find a more accurate value for the mean and variance.

## 7.3 Pairs Method

For both standard and reduced voltage settings 50 sets of pulses are recorded for the CalA analysis. The pair method involves taking single CalA shots from standard and lower voltage settings and fitting an exponential to the signal. The fitted exponential is used to find the mean value at the top of the signal and the variance around the fit. For each pixel 50 values for the Gain Variance ratio is found and this is repeated for the 440 pixels within the FD telescope.

Fig. 7.3 shows the average ADC count found across a camera for a FD telescope. The pattern follow how the camera is illuminated by the LED pointing at the camera. It shows that the spot is brightness in the middle and the intensity drops off towards the edges **need to add in diagram of labelled pixel no. across a FD camera**. There are uncertainties on the averages but are smaller than the displayed points. The variance measured in Fig. 7.5 shows an expected pattern too. The variance is proportional to the mean and is expected to follow a similar shape. This will not be exact but a good indicator of whether the variance was calculated correctly.

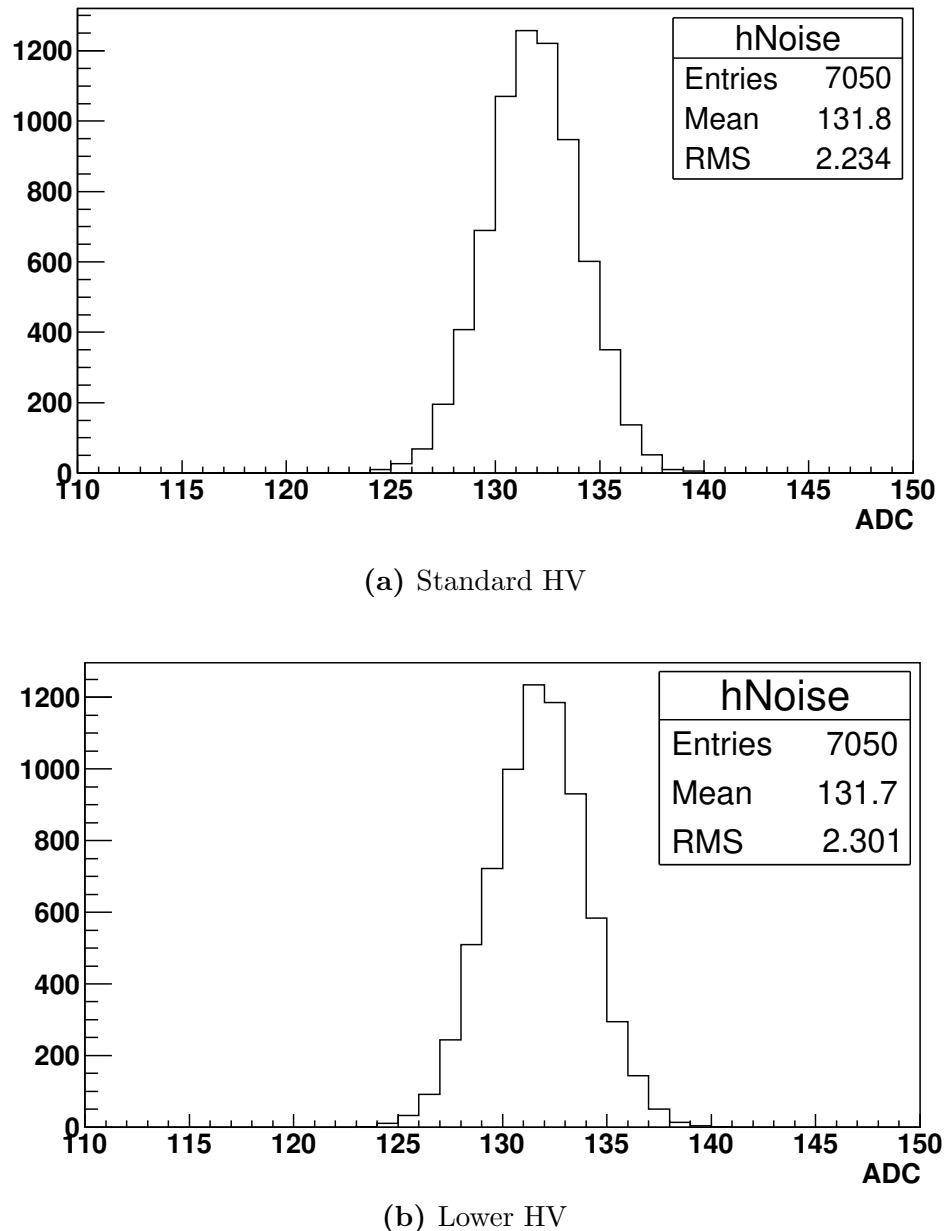


**Figure 7.1:** Sample of the observed electronic noise observed for a single pixel within Los Leones telescope 4. Electronic noise outside of the PMT so will be the same separate from the HV setting across the PMT.

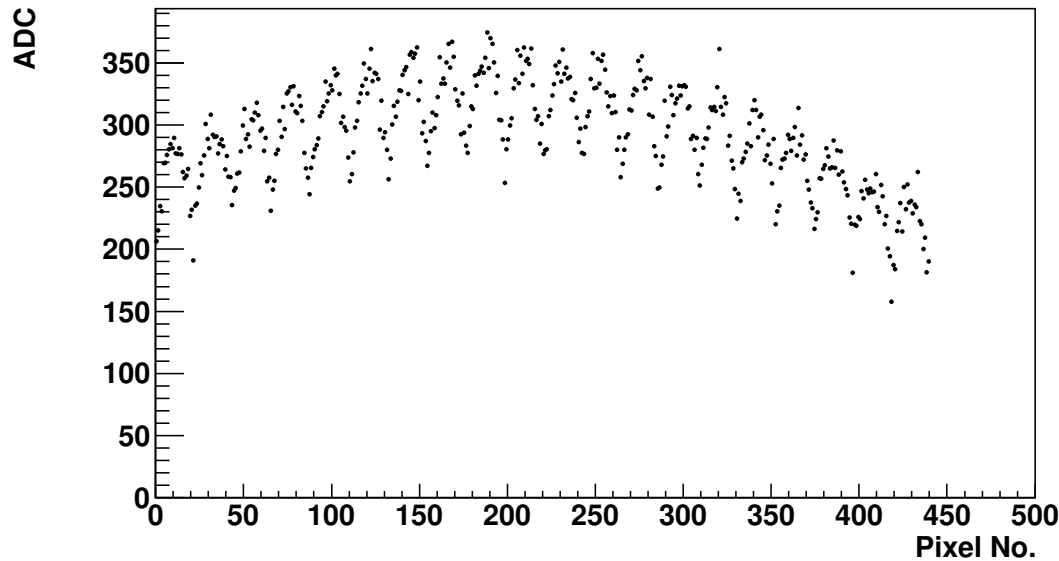


**Figure 7.2:** Mean measured at Standard HV for Los Leones Mirror 4. CalA data taken on the 11-06-2016.

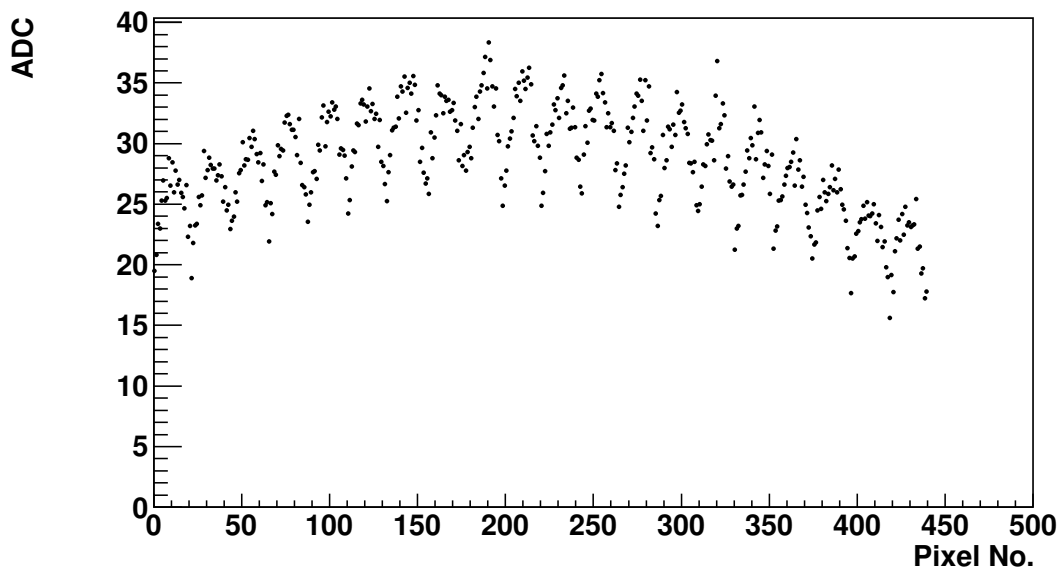


**Figure 7.3:** Mean measured at Lower HV for Los Leones Mirror 4. CalA data taken on the 11-06-2016.

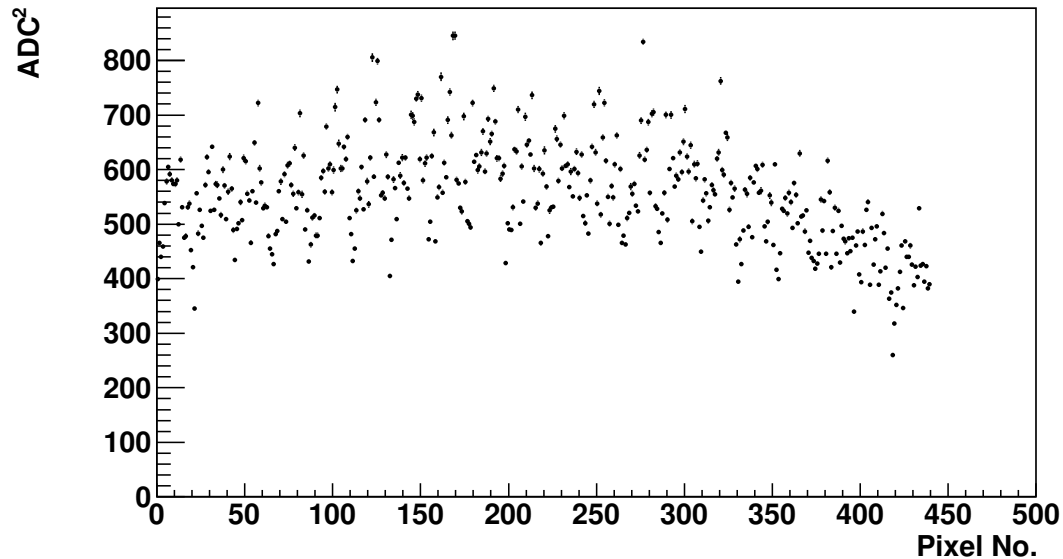


**Figure 7.4:** Variance measured at Standard HV for Los Leones Mirror 4. CalA data taken on the 11-06-2016.

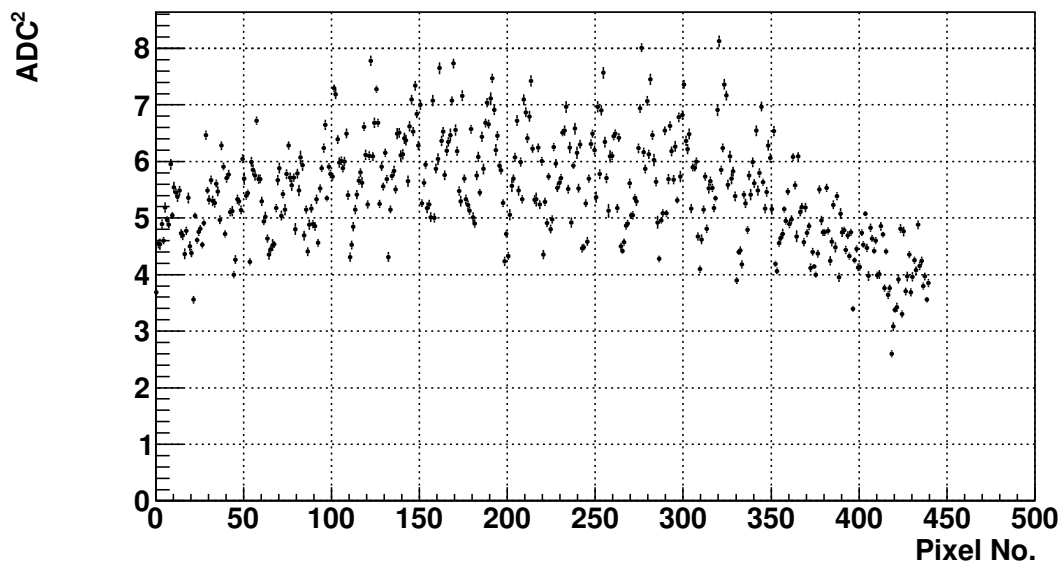


**Figure 7.5:** Varaince measured at Lower HV for Los Leones Mirror 4. CalA data taken on the 11-06-2016.

### 7.3.1 Results

Fig. 7.6 and Fig. 7.7 shows a demonstration of using the Pairs Method to calculate the Gain Variance Ratio. The CalA data used was taken on the night of the 11-06-2016 by Los Leones Mirror 4. The mean value in Fig. 7.6 shows a 3.7% change in the ratio which translates to a 10% change in the actual value of the PMT gain variance.

Fig. 7.7 shows the gain variance ratio measured per pixel. There can be seen no major structure or pattern. This is desired as the Gain variance is tied to individual PMTs and it would not be a great sign if the ratio followed a pattern like what was seen for the means and variances.

## 7.4 Averaging Sets of Traces Method

Instead of calculating the Gain Variance ratio on pairs of CalA traces then finding an average value the 50 traces for each set are stacked. This forms an average trace consisting of the 50 traces. To find the mean and variances of the noise a linear line of form  $f(x) = x$  is fitted to the first 140 bins. The fitted  $x$  is used as the mean and the variance is calculated around this value. Next an exponential is fitted to the signal. The value of the fit at the top of the signal is used as the mean while the variance is calculated around the fitted exponential.

### 7.4.1 Results

There is a larger spread in the histogram of calculated Gain Variance ratio than when the Pairs Method was employed. One good property is that no visible structure or pattern can be seen. There are definitely some extreme values of the ratio measured. To see what could cause the large outliers I had a look at the reduced chi-square of the fitted function to the noise and signal. There was no obvious problems when looking at the chi-squares as a function of pixel number for the signal. Examples are shown in Fig. 7.14 and Fig. 7.15. Examining the reduced chi-square of the fits to the noise it was seen that there were some large values. This was shown in Fig. 7.16 and Fig. 7.17. What was causing these weird fits was one or more of the noise bins having a larger deviation than expected from the measured average. **Add in plot showing off this behaviour.** This led to the process of investigating whether Least Trimmed Squares would be useful.

## 7.5 Result of Averaging Sets of Traces Method with Least Trimmed Squares

Least Trimmed Square is the method that involves removing points that have the greatest sigma away from an initial fit. A point is removed one at a time with the fit repeated and the reduced chi-square checked. This method is repeated until the reduced chi-square is below a threshold.

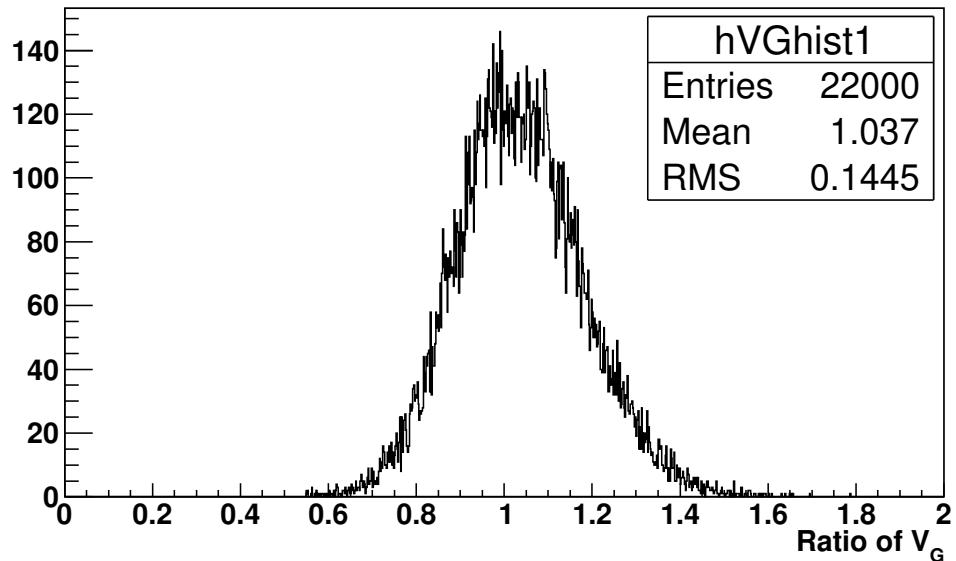


**Figure 7.6:** Histogram of the all the pairs methods for Los Leones Mirror 4. CalA data was taken on the 11/06/2016 at both Standard and Lower gain settings. There are 50 traces for each of the 440 pixels recorded at both gain settings.

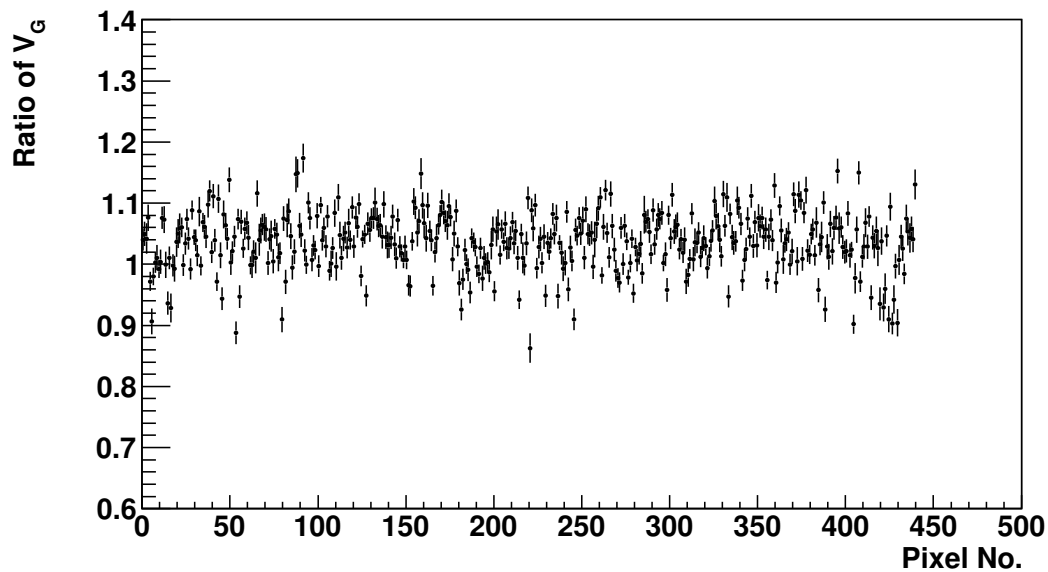


**Figure 7.7**

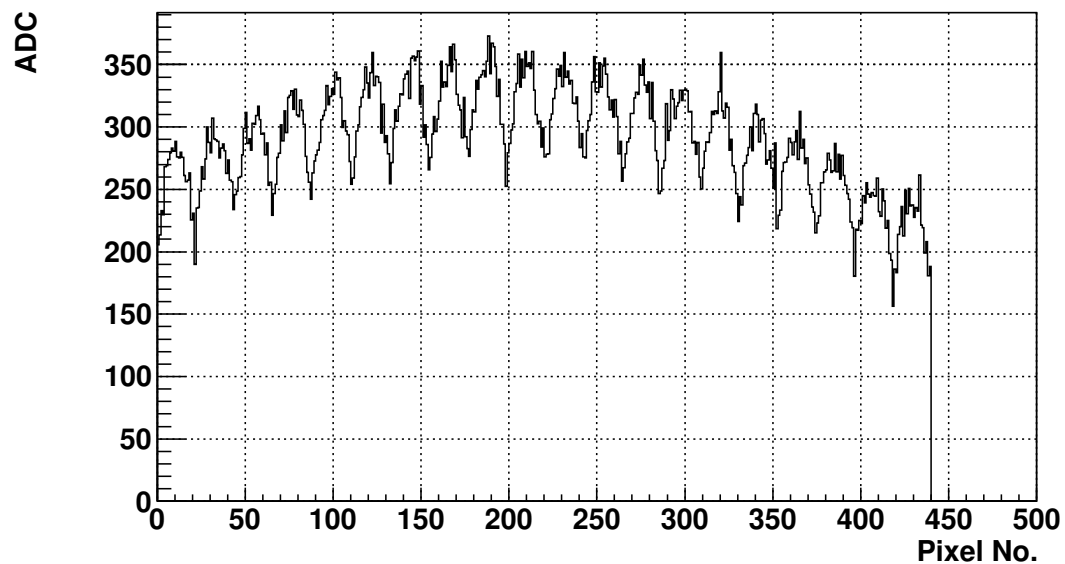


Figure 7.8

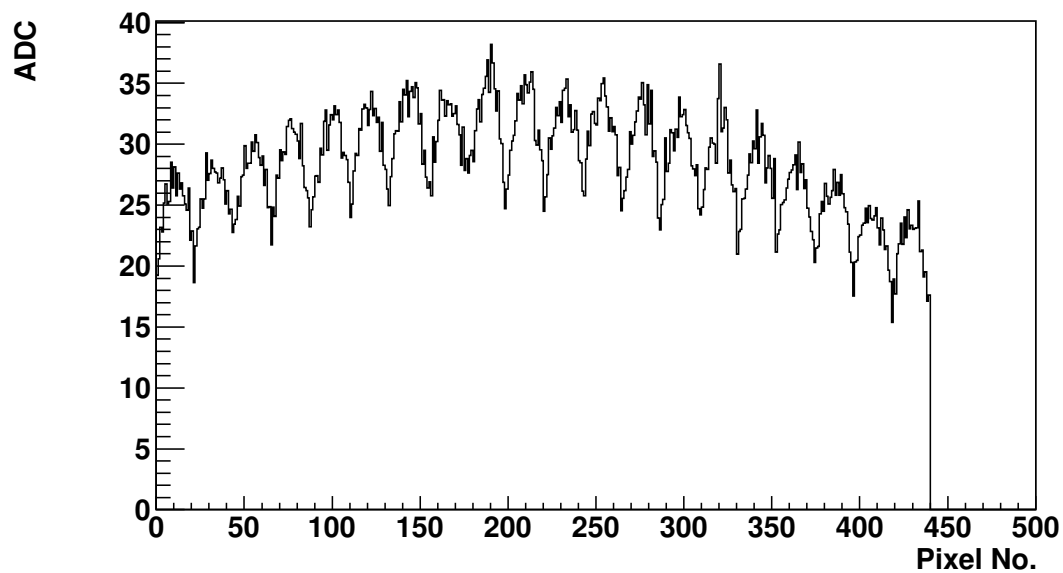


Figure 7.9

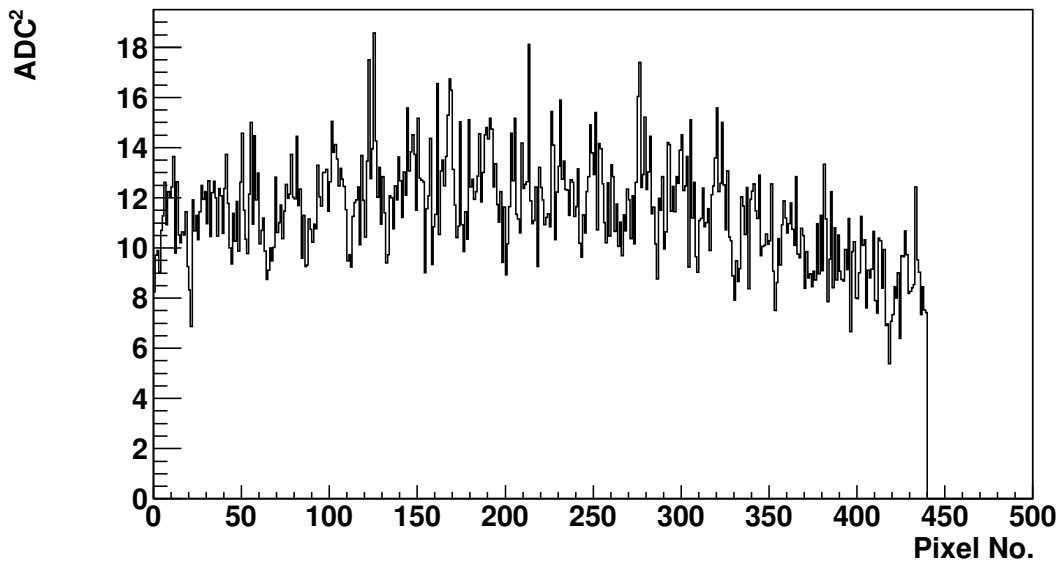


Figure 7.10

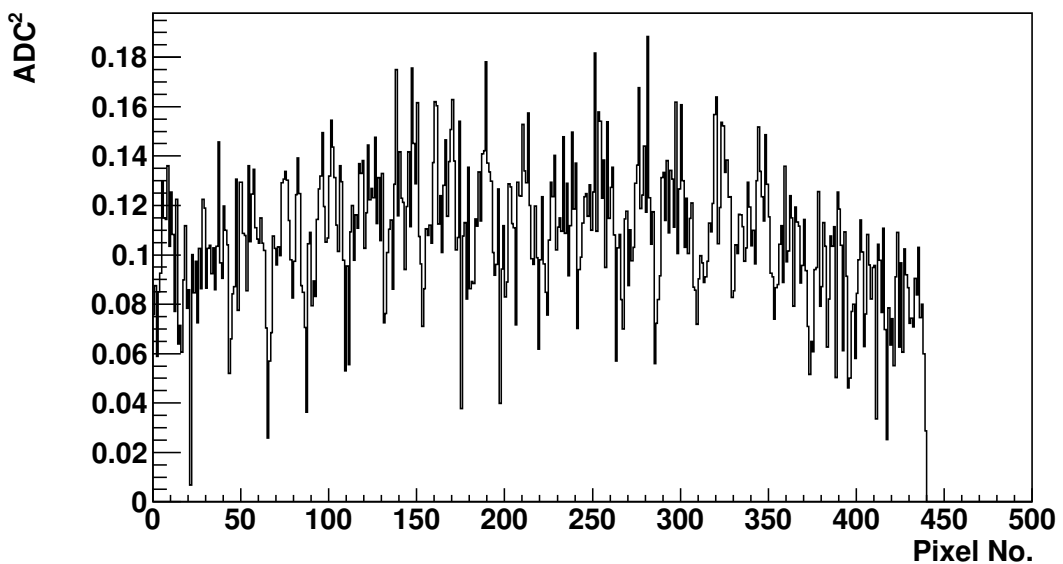


Figure 7.11

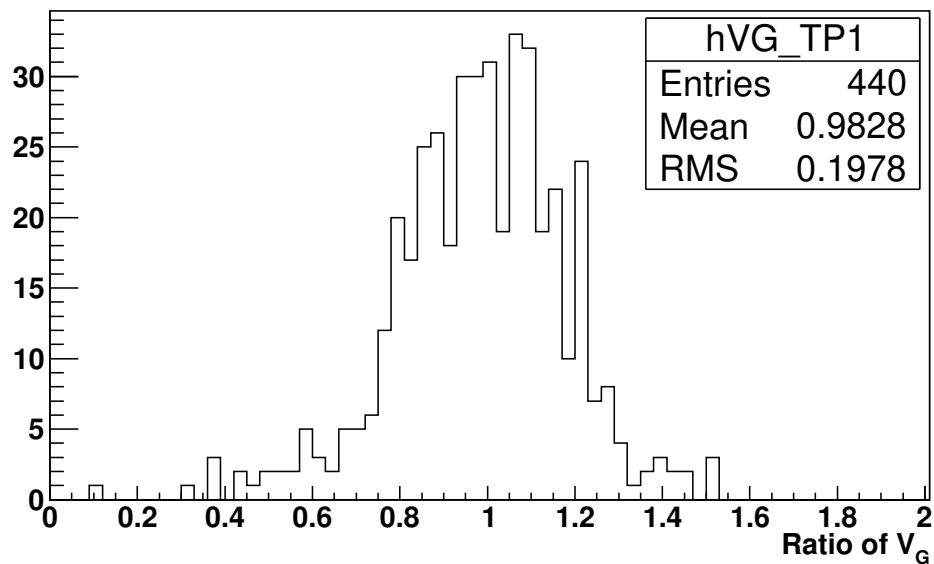


Figure 7.12

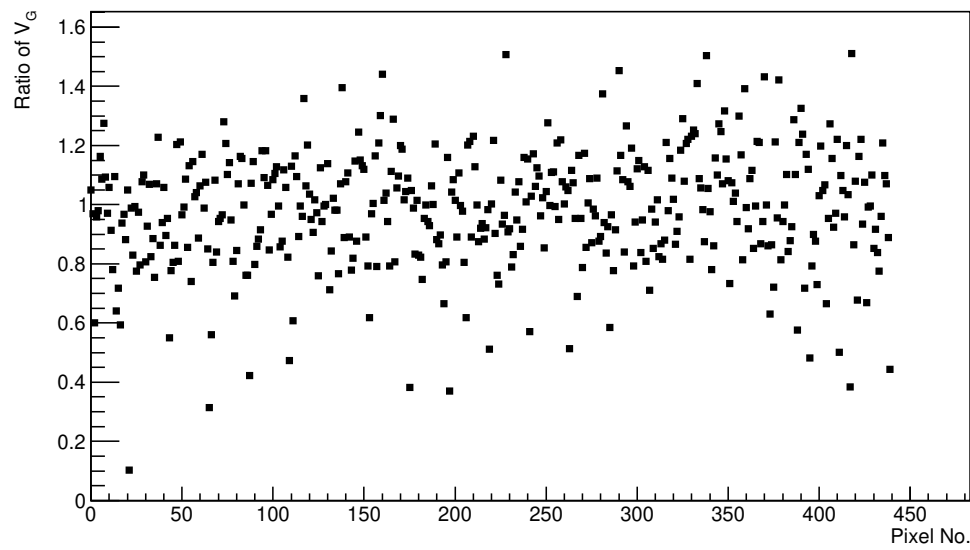
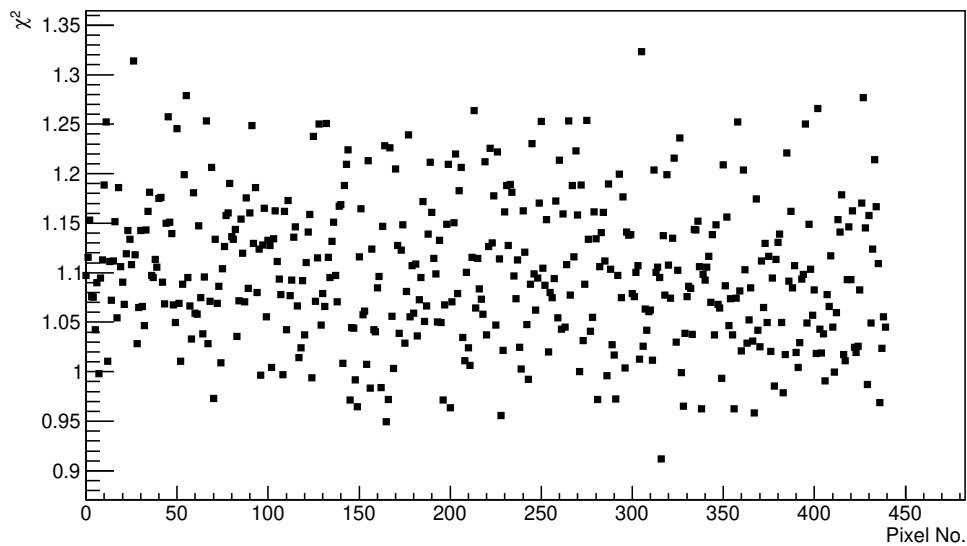
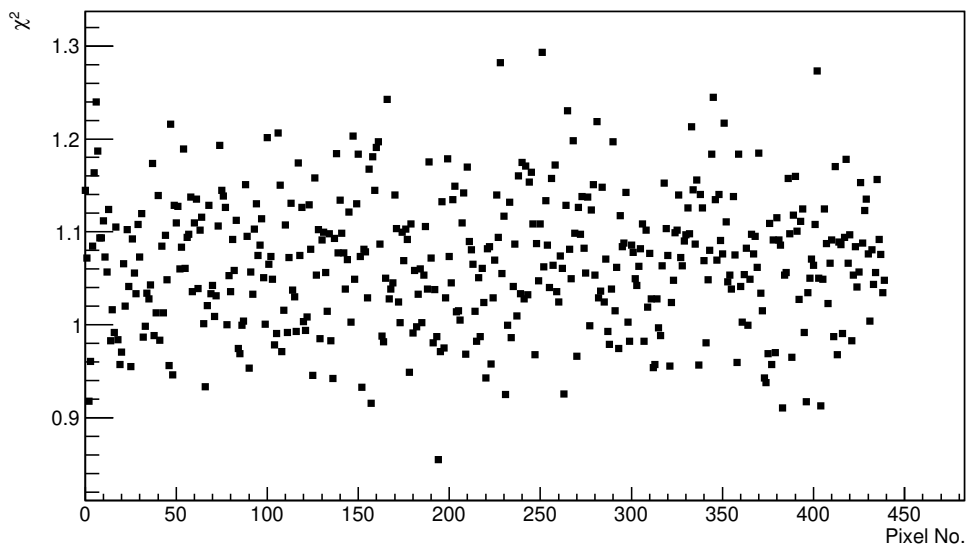


Figure 7.13



**Figure 7.14:** Reduced Chi-square for fitted exponential on the signal for CalA events measured at Standard HV.



**Figure 7.15:** Reduced Chi-square for fitted exponential on the signal for CalA events measured at Lower HV.

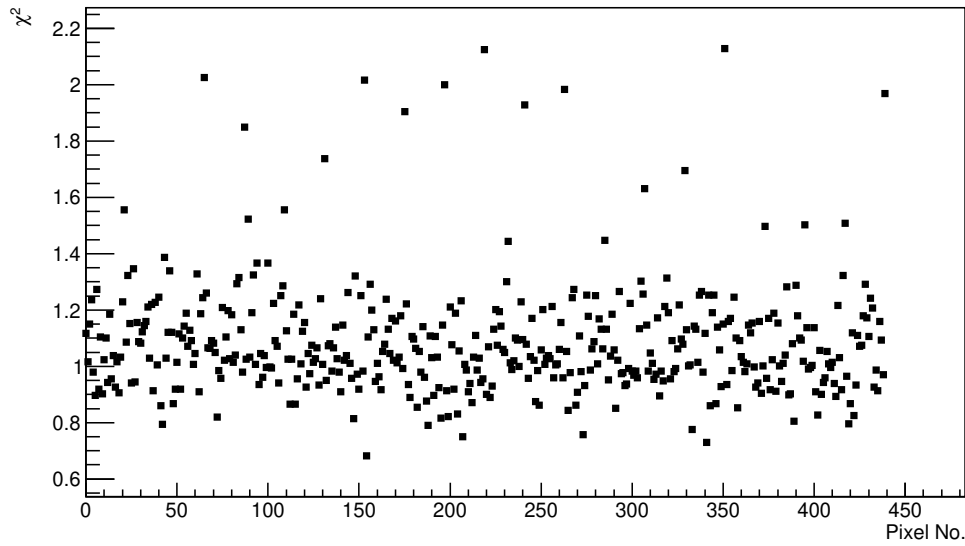


**Figure 7.16:** Reduced Chi-square for fitted line on the signal for CalA events measured at Standard HV.

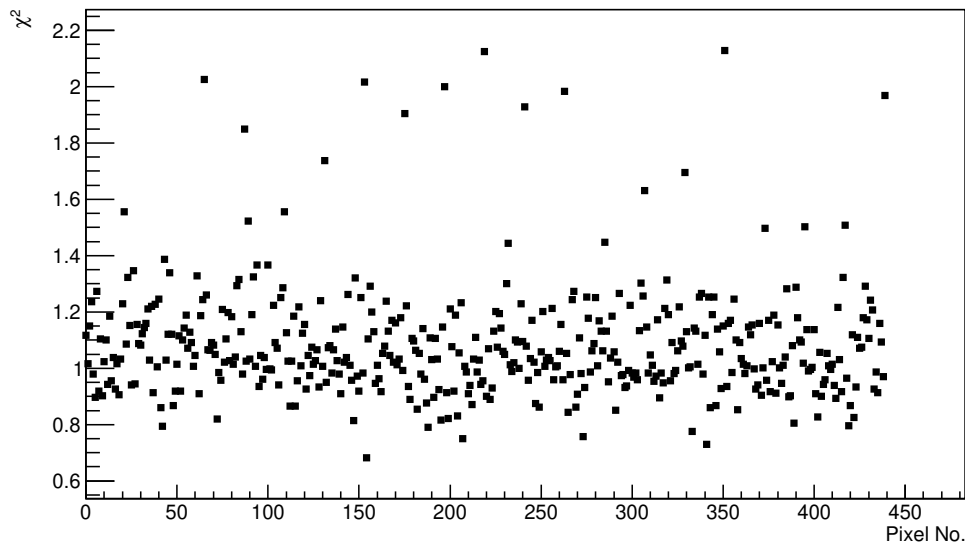


**Figure 7.17:** Reduced Chi-square for fitted line on the signal for CalA events measured at Lower HV.

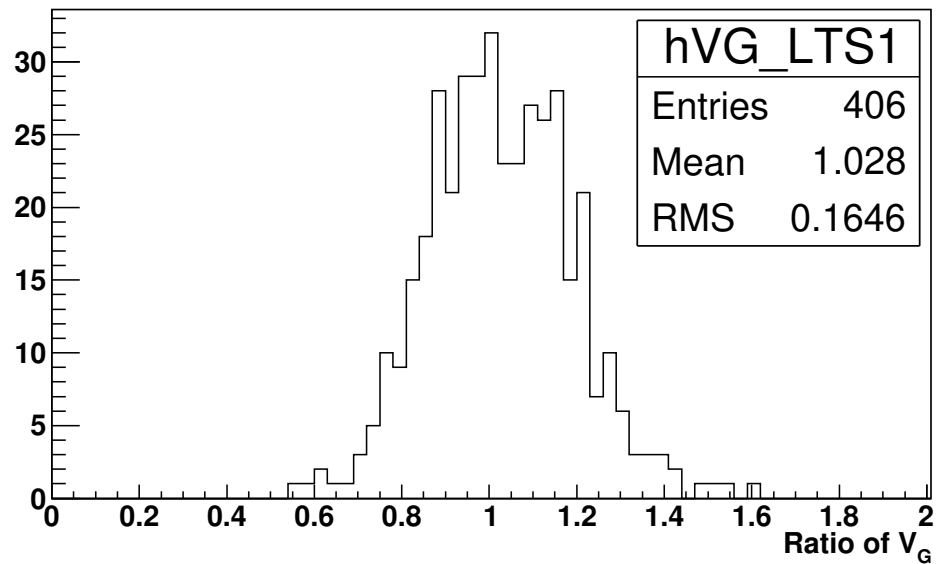


Figure 7.18

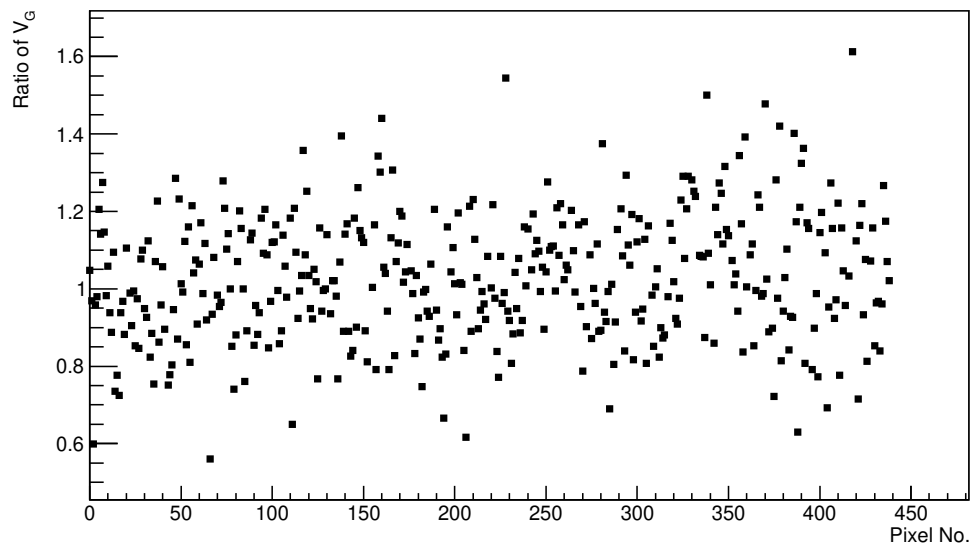


Figure 7.19

**7.6 Result of Averaging Sets of Traces Method using Noise Distribution**

**7.7 Attempts to measure Gain Variance directly in the Lab**

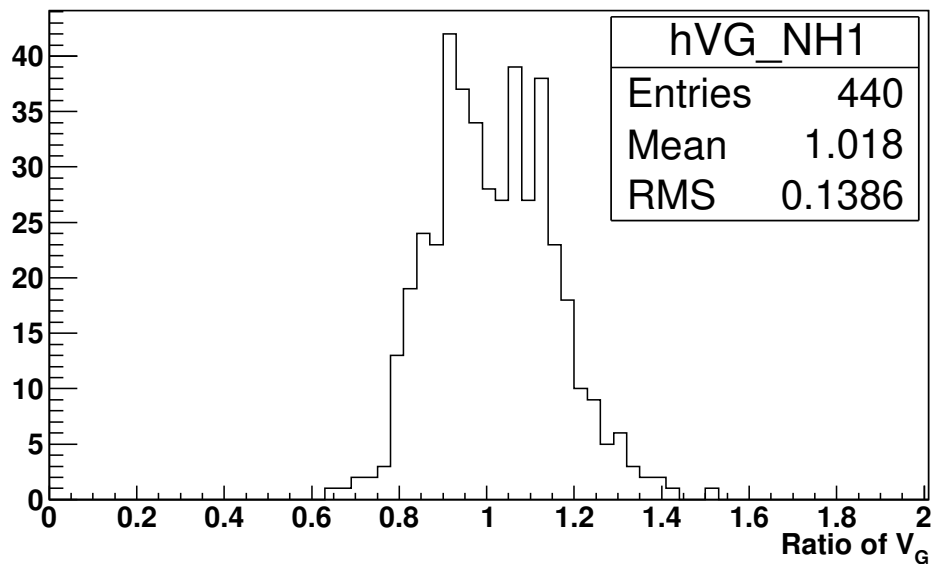


Figure 7.20

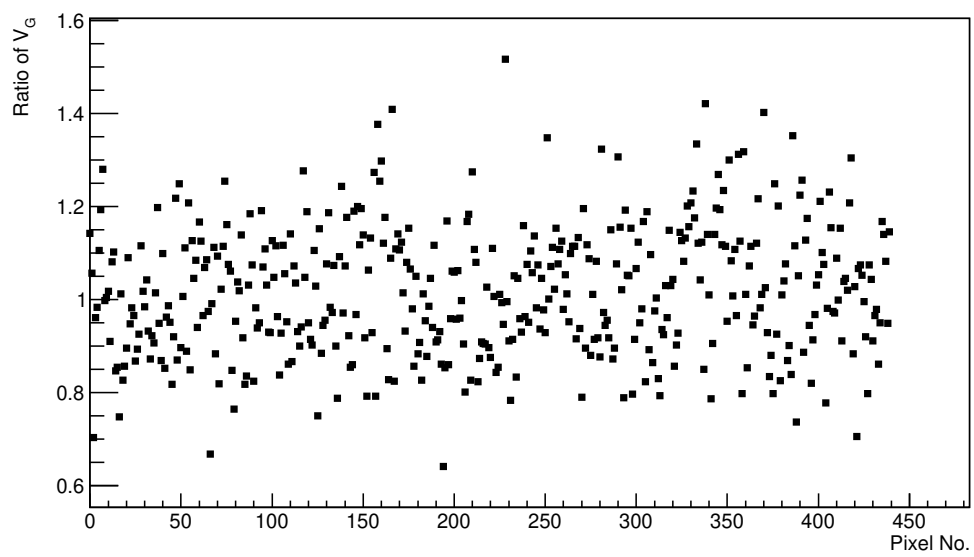


Figure 7.21



## Chapter 8

# Laboratory Simulation of FD shift

Laboratory Simulation of FD shift under differing NSB levels.

- Measurements for both 900V and 600V (900V used as baseline)
- Different length shifts
- Changing NSB
- measuring how the relevant Gain changes throughout a run



## Chapter 9

# Evaluation of Cloud Camera Cuts

First look into the effectiveness of the Cloud Camera cuts on PAO Golen Hybrid data.

- Are we being too conservative?
- Effects on Xmax, Zenith and Rp distributions



# **Chapter 10**

## **Conclusion**

### **10.1 Future Work**



# Bibliography

- [1] W. Heitler, *The quantum theory of radiation*. Oxford: (Clarendon Press, Ed. 3, Oxford), 1954.